CHAPTER 4

RESULTS AND DISCUSSION

Chapter 4.1

Development and Characterization of Copper Nanoparticles incorporated Chitosan and Gelatin based scaffold

4.1. Results and Discussion

To evaluate the mechanical strength and antibacterial properties of copper nanoparticles for tissue engineering applications we developed chitosan/gelatin based scaffold incorporated with copper nanoparticles and we compared their properties before and after seeding with L979 cells. The product parameters were established to identify the most suitable scaffolds that closely mimic the characteristics of the skin, making them ideal for skin tissue engineering applications.

As discussed previously also, chitosan is derived from chitin and is one of the most attractive natural biopolymers as it is hydrophilic, causes fibrous encapsulation, promotes cell adhesion and growth and also is anti-inflammatory in nature (Muzzarelli et al.,1994; Seol et al.,2004). Gelatin which is derived from collagen, is another well-researched naturally occurring biomaterial that encourages cell adhesion, proliferation, migration, and differentiation (Santoro et al.,2014; Strobel et al.,2017). It also has the Arg-Gly-Asp (RGD) sequence from collagen (Mao et al.,2003; Huang et al.,2005). Therefore, the chitosan/gelatin blends are very popular among researchers due to their biocompatibility, biodegradability, and low antigenicity, as reported in prior studies to enhance the biological response when compared to pure chitosan (Huang et al.,2005). This has resulted in positive outcomes in tissue engineering applications, including skin (Tseng et al.,2013), cartilage (Xia et al.,2004; Wang et al.,2009), and bone regeneration (Miranda et al.,2011). Unfortunately, the chitosan/gelatin scaffold architectures' fragility in aqueous solutions limits their use in bone tissue engineering. However, the blending of metallic nanoparticles and bioceramics has received great attention in recent years to improve the mechanical properties and bioactivity of this chitosan/gelatin combination. Copper nanoparticles have demonstrated great significance in tissue engineering applications due to their antibacterial properties, mechanical properties, angiogenic and osteogenic potential. It upregulates the gene expression of vascular endothelial growth factor, to stimulate the biological properties necessary for endothelial cell proliferation during wound healing and it also promotes the mesenchymal stem cells' differentiation into osteoblasts (Klatte-Schulz et al., 2012). Considering the above, copper nanoparticles were chosen to form a nanocomposite scaffold with chitosan/gelatin blend of improved mechanical strength and wound healing properties. Besides material properties, the fabrication of scaffolds with porous architecture was another important aspect, which can mimic the body tissue. Therefore, lyophilization was utilized as the most suitable method for the generation of porous nanocomposite. The research work in this phase of the thesis focuses on the development and characterization of a novel

Ch/G-CN nanocomposite scaffold for skin tissue engineering application. The scaffolds were subjected to morphological, physicochemical and *in vitro* biological characterizations to prove their potential to act as cell careers for skin tissue regeneration. The results and discussion of these experimental studies are presented in this chapter.

4.1.1. Morphological analysis of Copper Nanoparticles (CN) with EDX

HRSEM was done to analyze the surface morphology of the nanoparticles synthesized. Fig.4.1.1a shows the clusters of nanoparticles formed because of the agglomeration that occurred in the free state of the nanoparticles. However, it showed the presence of heterogeneous sizes of particles formed capped with starch it was not clear from the image that these are copper nanoparticles. Therefore, EDS spectra helped us determine the elemental composition of the synthesized nanoparticles. Fig.4.1.1b indicated the presence of CN while some traces of O and C were also found which were due to the application of starch as a stabilizer in the experiment. Peaks found at binding energies of 0.98, 8.09 and 8.99 keV confirmed the existence of a copper (Karp et al., 2003). To confirm this further we performed more characterization of the synthesized nanoparticles.

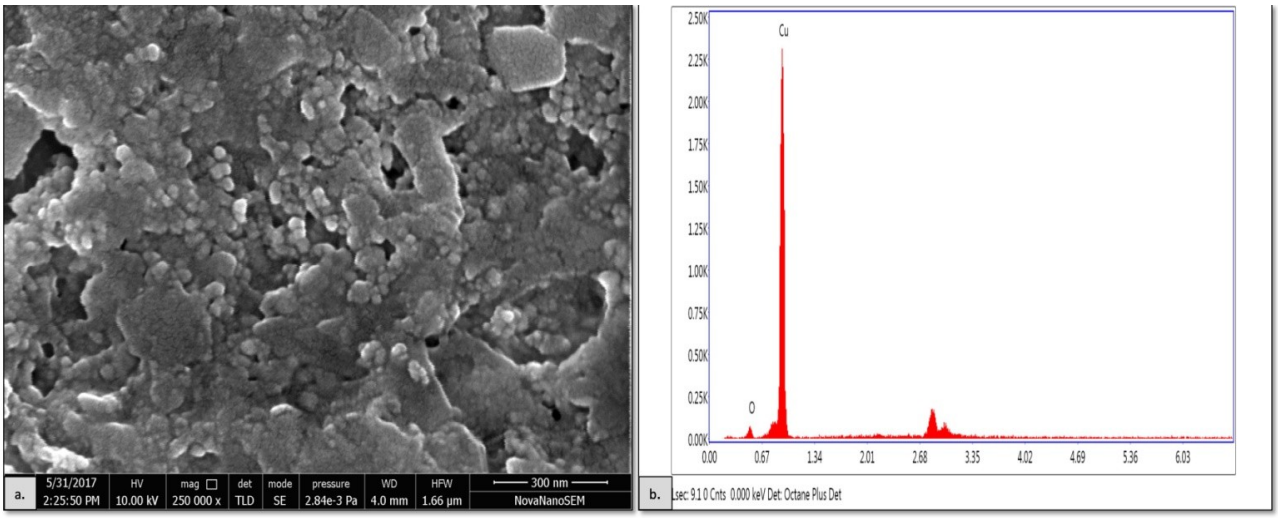

Figure 4.1.1(a): HRSEM image of synthesized copper nanoparticles from chemical reduction method.
Fig.4.1.1(b): EDS graph for synthesized copper nanoparticles

1.1.2. Structural characterization of synthesized Cu nanoparticles

X-Ray Diffraction

XRD analysis was further performed to analyze the crystal structure and size of the synthesized nanoparticles. Fig.4.1.2. shows the XRD pattern of copper nanoparticles. Peaks observed at 2θ values of 43.33°, 50.45° and 74.10° correspond to h, k and l values 111, 200 and 220 planes of

metallic Cu. It was confirmed by JCPDS card no. 04-0836 for standard spectrum face-centred cubic metallic Cu. The mean size of the Cu nanoparticles calculated from the major diffraction peaks using the Scherrer formula is about 25.318 nm, respectively. Broadening of the peak in the XRD pattern shows the presence of small nanoparticles (Yang et al., 2001).

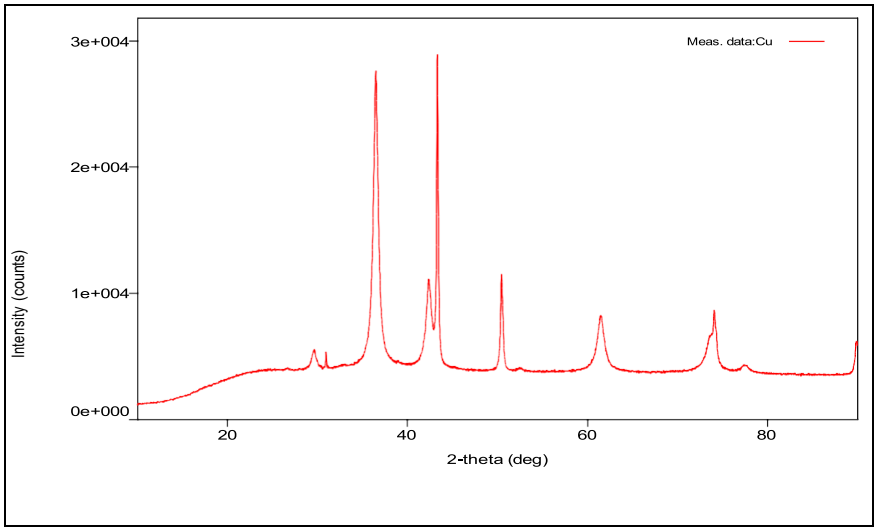

Figure 4.1.2: XRD spectra of synthesized Cu nanoparticles showing its structural composition

Transmission Electron Microscopy

HRSEM defines only the surface morphology of the nanoparticles hence it was important to do the TEM analysis to find the internal composition of the synthesized nanoparticles. Fig.4.1.3a shows the TEM of nanoparticles synthesized, the average size of nanoparticles found from this analysis is 5.31nm and the particles are very well dispersed. It is also clear from TEM that the nanoparticles formed are very small in size (Sarkar et al., 2013). The diffraction pattern of TEM for copper nanoparticles is shown in Fig.4.1.3b. As the nanoparticles are very small in size therefore only certain dots of circular shape are visible in them which confirms the crystalline structure of the copper nanoparticles synthesized (Rajesh et al.,2018).

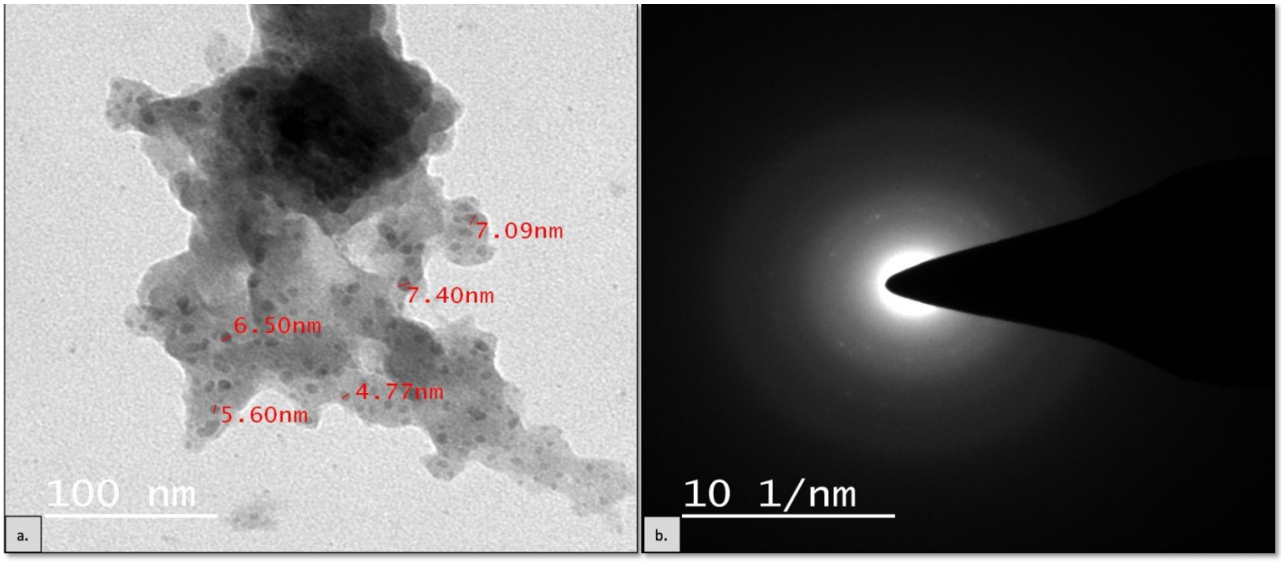

Figure 4.1.3(a): TEM micrograph of synthesized CN nanoparticles.
Fig.4.1.3(b)- SAED pattern for synthesized CN nanoparticles showing the shape of nanoparticles formed

4.1.3. Functional characterization of synthesized Cu Nanoparticles (FTIR)

Furthermore, FTIR analysis was done for the copper nanoparticles to obtain functional characteristics of the nature of nanoparticles. Fig.4.1.4 shows the FTIR spectra of copper nanoparticles synthesized. FTIR spectra of copper nanoparticles showed that the nanoparticles were surrounded by various organic molecules like carboxylic acid, alcohols, ketones and aldehydes. The broad band that was observed around 616 cm^{-1} depicts the stretching frequency of the OH group that was present on the surface of the copper nanoparticles. Other than that, peaks were observed at 3366.60 cm^{-1}, 2920.18 cm^{-1}, 1369.50cm^{-1} and 1265.35 cm^{-1} corresponding to O-H stretching, C-H stretching vibrations in CHO and phenols, C-H bending of methyl groups and C-O stretching alcohols, ethers respectively. Peaks at 1624.12cm^{-1}, and 1072.46cm^{-1} correspond to the C=O stretching vibration due to starch capping over copper nanoparticles, and the latter corresponds to the C-O stretching vibrations or C-O-C stretching vibrations of ascorbic acid. 505.37 cm^{-1} peak in the spectra corresponds to the Cu-O stretching vibration depicting the oxidation of copper here (Betancourt- Galindo et al., 2014).

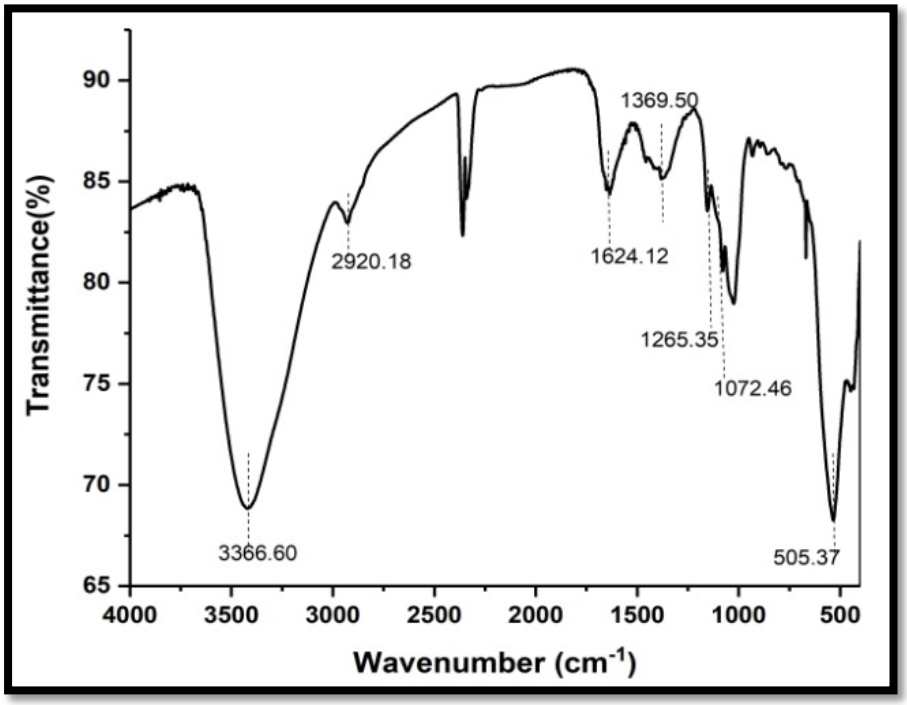

Figure 4.1.4: FTIR spectra of synthesized CN nanoparticles showing different functional groups interaction

4.1.4. Fabrication and Characterization of Ch/G and CN incorporated Ch/G scaffolds

Morphological evaluation

The prepared Ch-G scaffolds appeared as spongy materials. These scaffolds were brownish-white in colour. The brown colour may be associated with the colour of the chitosan, whereas, the whitish tinge is associated with the gelatin. An increase in the chitosan proportion within the scaffolds increased the brownish touch. More firmness and strength were added to the scaffolds by the addition of gelatin to the chitosan solution in varied proportions. Fig.4.1.5 shows the digital images of developed scaffolds without copper nanoparticles and with copper nanoparticles. The colour of the scaffolds changed from brownish-white to greenish-white after the addition of CN into the Ch/G solution in different concentrations. It was also seen that the stiffness and firmness of the scaffold gradually increased in 1:1 and 1:2 ratios of Ch-G scaffold after the addition of 0.01%CN and 0.03% CN into the scaffolds respectively. Porous structure was also evident in the figures after the addition of CN into the scaffolds as a lyophilization process was adopted to fabricate these scaffolds.

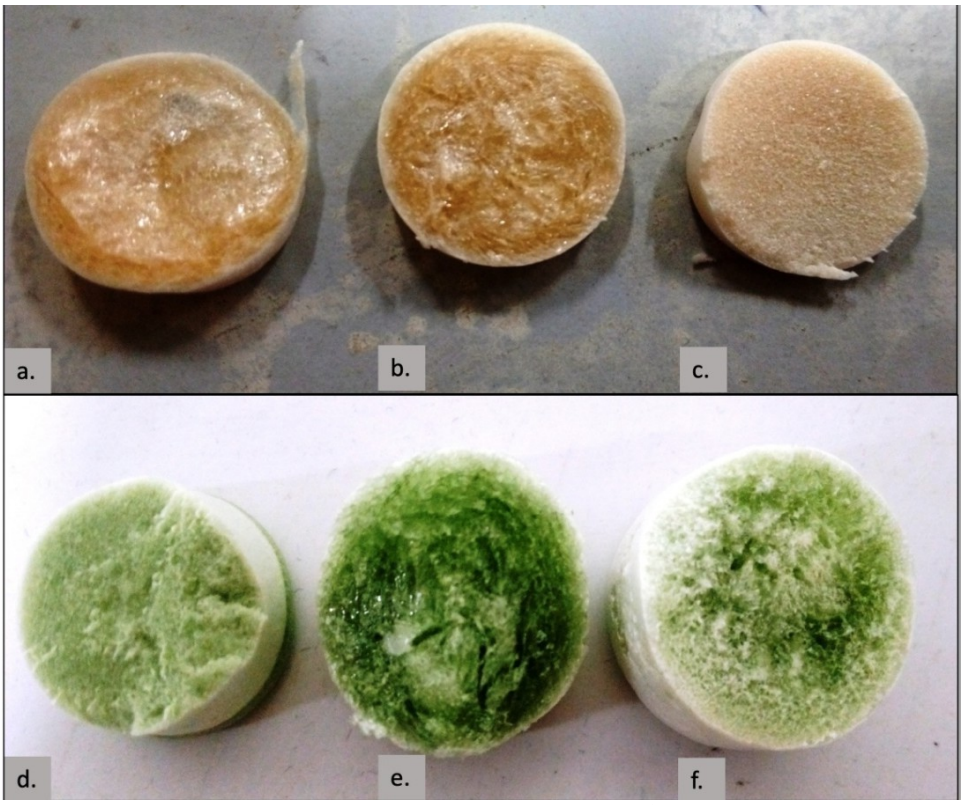

Figure 4.1.5: Digital image of scaffolds without CN and with CN. Figure 4.1.5(a-c): Digital images of Chitosan gelatin scaffold with 1:1, 1:2 and 1:3 ratio of Chitosan and gelatin. Figure 4.1.5(d-f)): Digital images of Chitosan gelatin scaffolds with 0.01%, 0.02% and 0.03% CN respectively from left to right.

Scanning Electron Microscopy

The morphological characteristics of the scaffolds were determined by SEM. It also helped in determining the appropriate pore size distribution. These images show that the average pore size of the scaffolds is 35µm which is quite good for skin cell infiltration (Yannas et al., 1989). The large surface area of the obtained scaffolds is clear in the SEM images. SEM images of porous scaffolds revealed the interconnectivity of the porous structure and it also exposed the smooth and homogenous pore walls surface. Fig. 4.1.6 shows the SEM images of the scaffolds of different compositions of chitosan/gelatin and also after the addition of copper nanoparticles. The average pore size for the scaffolds formed after the incorporation of copper nanoparticles is about 71 µm which again proves to provide better strength to the scaffold and also to the cells. It is also proved that the fabrication technique affects the pore size distribution and structure of scaffolds. Hence it can be said that the freeze-drying technique proved to be a beneficial asset in obtaining good pore size and interconnectivity of pores (Hilmi et al., 2013).

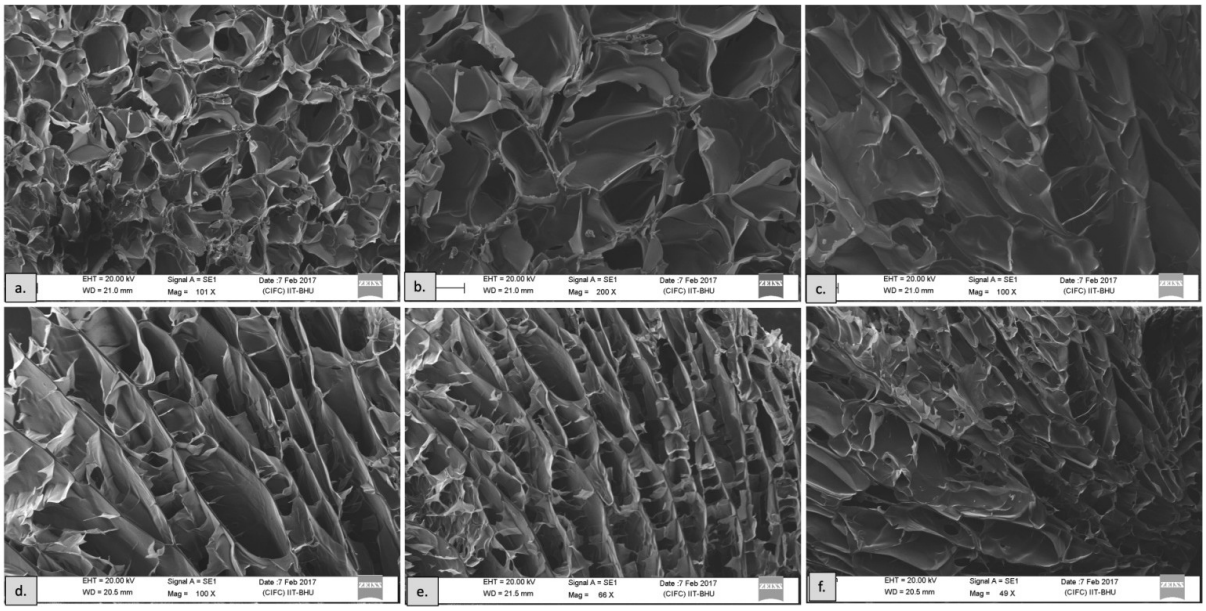

Figure 4.1.6(a-c): SEM images of Chitosan/Gelatin scaffolds.
Fig 4.1.6(d-f): SEM images of Chitosan/Gelatin scaffolds with 0.01CN, 0.02CN and 0.03CN

Structural and functional analysis of Ch/G scaffold and Ch/G-CN scaffolds

XRD pattern of various scaffolds is shown in Fig.4.1.7 which indicates different peaks corresponding to chitosan and gelatin blend and also chitosan-gelatin copper nanocomposite. The peak bend at approximately 20.53 keV is quite prominent in all six plots depicting the presence of chitosan. It corresponds to lattice plane 211. This bend has been increasing for quite a long which represents the blend formed with gelatin. Gelatin is depicted, here in the plot by the broad bend at 19.37 keV which is because of a combination of gelatin and chitosan (Zhuang et al., 2015). Other than that, one more diffraction peak at 2θ around 19.37 keV is prominent in F4, F5 and F6 which corresponds to copper nanoparticles present in the scaffolds. Another peak is observed in F4 at 50.45 keV which again corresponds to copper nanoparticles. The sharpness of this peak is attributed to a higher degree of crystallinity.

FTIR analysis was performed to determine the functional groups present in the scaffold's component and analyze the chemical interaction occurring between the functional groups. Cross-linking was observed in the structures which showed different modifications in the structure therefore various bands and peaks were observed. Fig.4.1.7 shows the FTIR spectra for developed scaffolds prepared with CN and without CN. The FTIR spectra of all the samples showed a broad band around 3425cm^{-1} and a weak peak at 2900cm^{-1} which corresponds to CH_2 and OH group. While the band at 1640cm^{-1} and peak at 1594cm^{-1} depicts the existence of the C=O group of acetylated amide and amine groups (Xu et al., 2012). All three blend samples F1, F2 and F3 consist of the same functional groups, therefore, all their FTIR spectra exhibited

bands at 1640, 1540 and 1240 cm^{-1}. While in F4, F5 and F6 weak peaks at 1623cm^{-1} are observed which is exhibited by copper nanoparticles. Also, a sharp bend can be observed at 1260cm^{-1} which corresponds to copper interaction with chitosan and gelatin blend.

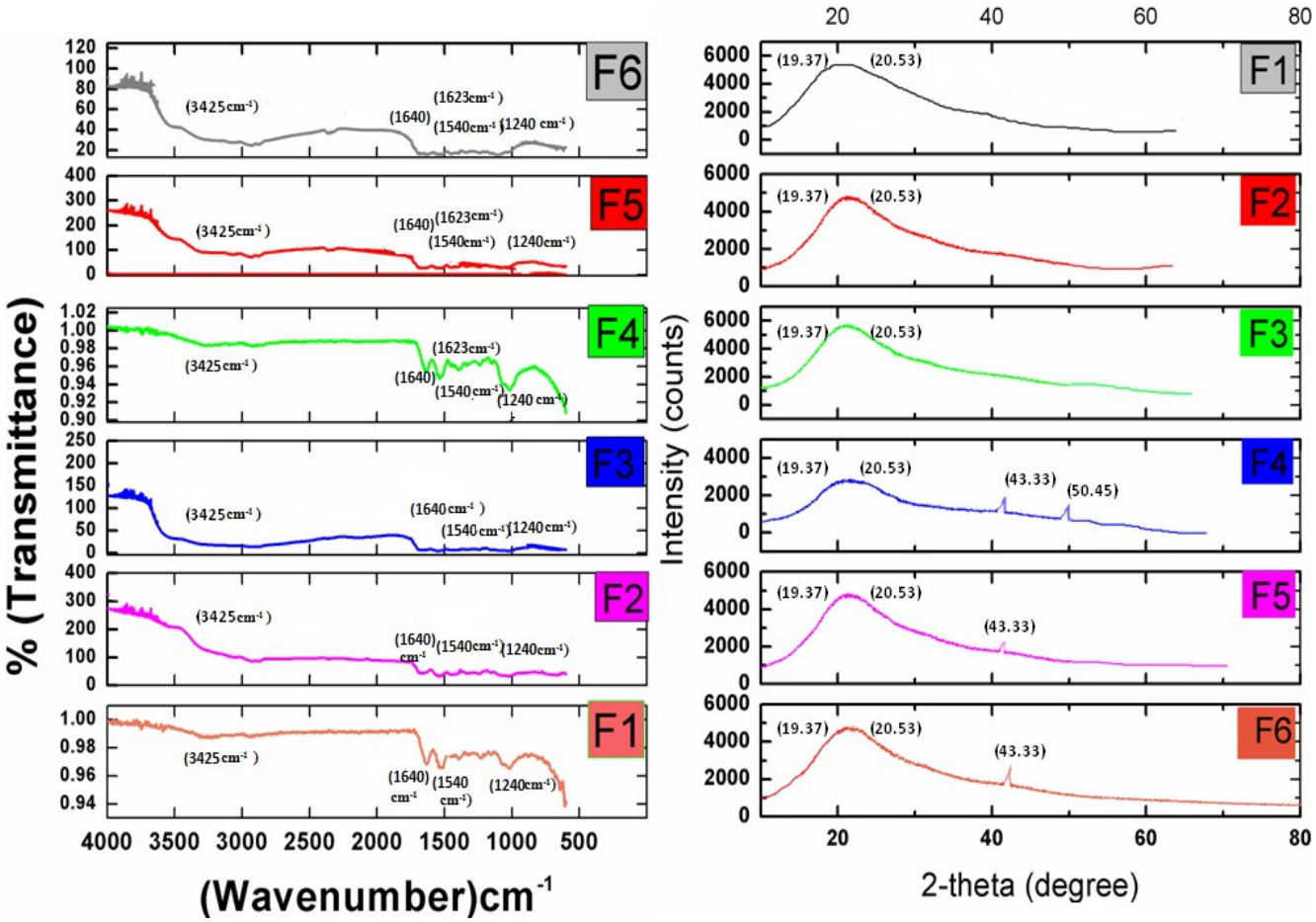

Figure 4.1.7: FTIR spectra and XRD spectra of developed scaffolds without copper nanoparticles and with copper nanoparticles

Mechanical strength evaluation

Fig.4.1.8 shows the mechanical strength of the developed scaffolds. This study showed that with an increase in gelatin concentration in the scaffolds the mechanical strength improved. However, an increased concentration of gelatin led to a higher degradation rate therefore an optimal gelatin concentration should be opted for further studies. It also shows that after the incorporation of the nanoparticles into the scaffold, the mechanical strength improved drastically. It was observed that after the incorporation of 0.03% CN into the scaffolds the compressive strength reached 3.12 ± 0.21MPa from 1.7± 0.11MPa (Ch-G3). It was also seen that it was highest in comparison to 0.01% CN and 0.02% CN incorporated scaffolds with 2.27 ± 0.045MPa and 2.75 ± 0.02MPa respectively.

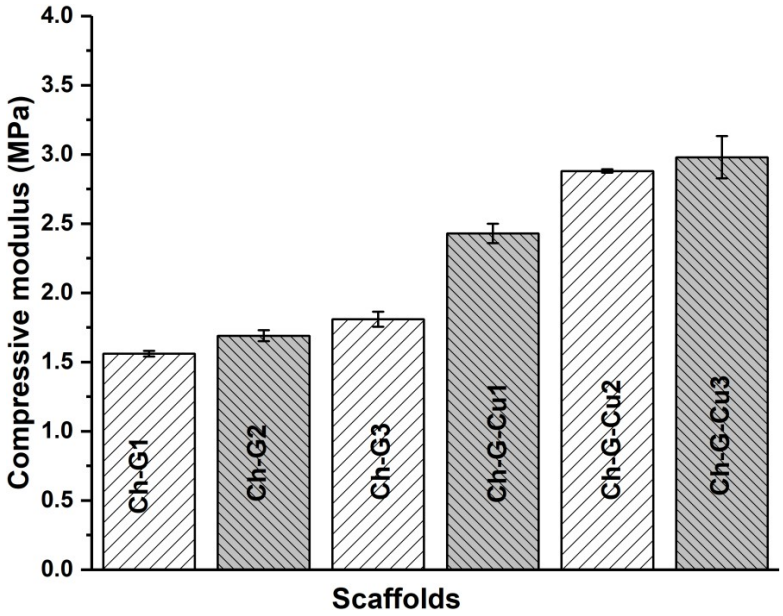

Figure 4.1.8: Mechanical strength analysis of developed scaffolds with and without copper nanoparticles

Swelling study

The swelling study revealed that after the incorporation of copper nanoparticles into the scaffolds, the water absorption capacity was reduced compared to the control scaffolds. Fig.4.1.9 shows the swelling ratio of the developed scaffolds. For Ch-G scaffolds with different percentages, the swelling ratio was higher in the range of 4.4 ± 0.044 to 5.2 ± 0.045 mg/mL while for 0.01CN-based scaffold, it reduced to 4.2 ± 0.032 mg/mL. It kept reducing till 3.8 ± 0.015mg/mL after continuous increments in the copper nanoparticles. It might be due to the surface modification occurring due to the addition of copper nanoparticles. The uniform dispersion of the nanoparticles over the surface of the scaffolds leads to a reduction in the swelling capacity of the scaffolds. Hence, it can be inferred from this study that the addition of copper nanoparticles reduced the swelling capacity of the scaffolds but it was the lowest in the case of 0.01CN nanoparticles and therefore it can be applied for further study.

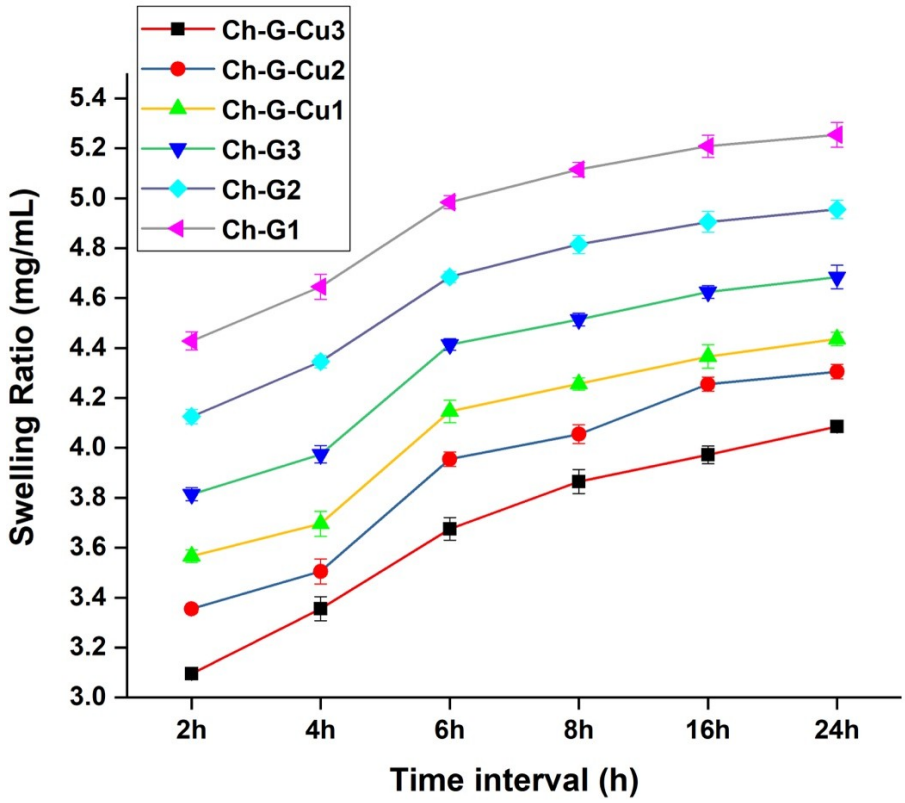

Figure 4.1.9: Graphical representation of swelling ratio of developed scaffolds with and without CN

***In-vitro* Biodegradation study**

Degradation occurs usually because of the dissolution of scaffolds that are exposed to PBS. It is very essential because it allows the cells to form their extracellular matrix (O'brien et al., 2011). In order to determine the scaffold's effect on the cell viability growth here within, Fig.4.1.10 represents the *in-vitro* degradation rates of the scaffolds. Fig.4.1.10 shows that F1, F2 and F3 are the control scaffolds for the copper-doped scaffolds i.e., F4, F5 and F6 respectively. It is visible from the plot that after the addition of copper nanoparticles the degradation rates have lowered to 37% approximately in comparison to the control scaffolds. In the case of chitosan-gelatin scaffold with 0.02% CN, the scaffolds have shown a much lower rate of biodegradation (15%) in comparison to scaffolds with 0.01%. It is also seen that the control scaffolds F2 and F3 without CN where gelatin concentration is higher show the highest rate of degradation i.e., 47% with respect to the control scaffold with 1:1 ratio of chitosan and gelatin. Hence it can be said that after the addition of CN, the rate of biodegradation has gradually dropped thereby making the scaffold best suitable for wound healing applications, as this is going to provide better strength and stability to the cells (Gurtner et al., 2008).

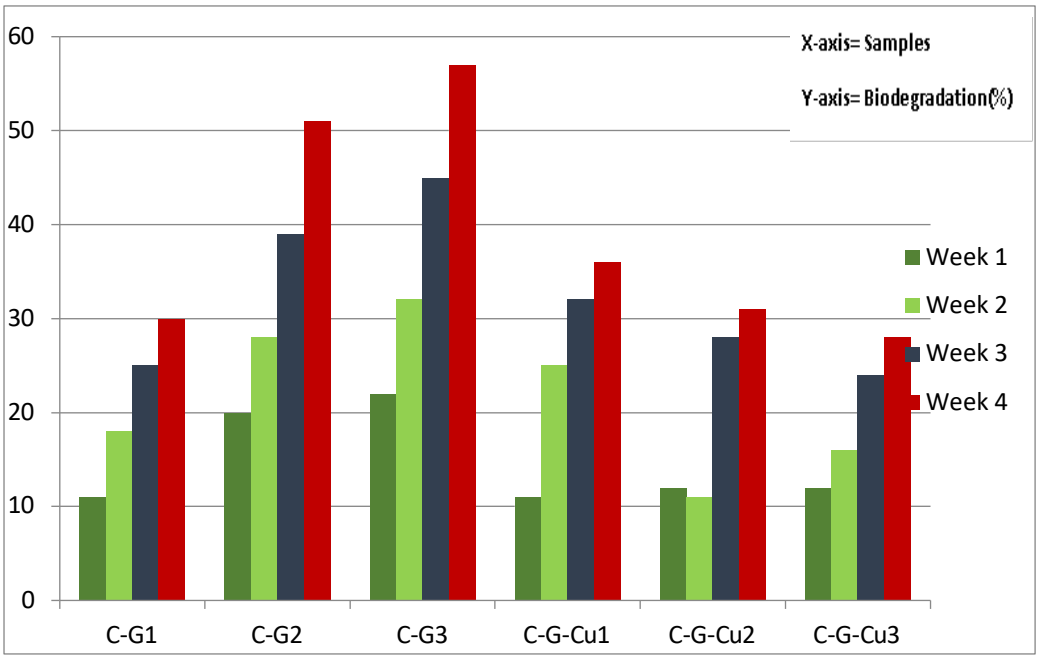

4.1.10: Biodegradation study (28 days) for developed scaffolds with CN and without CN

Porosity

The porosity of the scaffolds is depicted in Fig.4.1.11, which shows that with an increase in chitosan concentration, the porosity of the scaffolds is reduced. It is also clear from this graph that the scaffold with 0.01% Cu and with a 1:1 ratio of chitosan and gelatin has the highest porosity. This means that the Cu nanoparticles embedded scaffold with a 1:1 ratio of chitosan and gelatin is best suitable for cell proliferation and their attachment. The simultaneous addition of CN into the scaffold resulted in decreased porosity. This might have occurred due to the aggregation of the nanoparticles over the scaffold's surface and would have increased the compactness of the scaffold which ultimately led to the loss of interconnectivity of the pores. Uniform pore distribution can also be seen in the control scaffolds where the highest porosity is found in the chitosan and gelatin scaffold with a 2:1 ratio i.e., with an increase in chitosan concentration porosity of scaffolds has also increased. This may be associated with the water uptake rate by the scaffold because it generally depends upon the size and number of pores. This may be an important aspect of a scaffold developed specifically for wound healing applications because a moist environment is essential for a wound to heal completely.

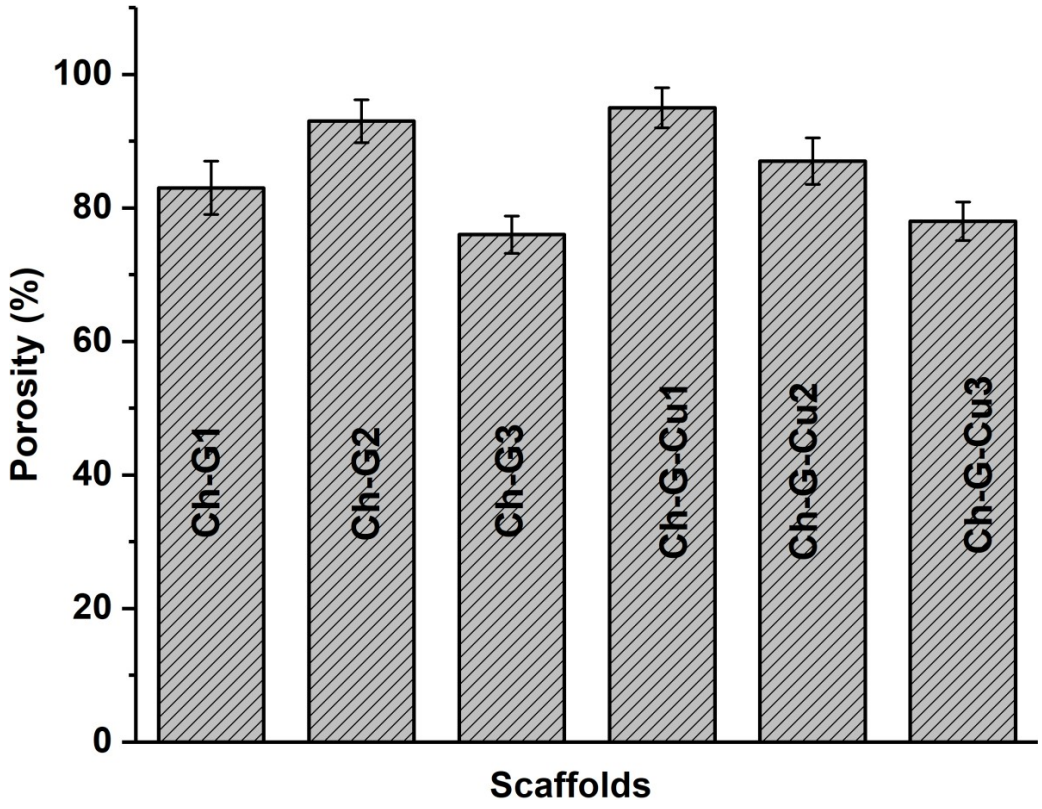

Figure 4.1.11: Graphical representation of porosity of developed scaffolds with and without Cu Nanoparticles

MTT assay

All the above assessments taken together, CN/ Ch/G composite scaffold was found to possess a desired set of superior scaffold properties namely porosity, mechanical strength, biodegradability and swelling ratio and hence it was selected for *in-vitro* cell study to evaluate its potentiality for tissue regeneration.

The MTT assay showed that scaffolds with a copper concentration of 0.01% showed a higher proliferation rate among all the scaffolds. But chitosan and gelatin scaffolds with a 1:1 ratio also proved to have better cell viability in comparison to other control scaffolds. At the end of the 7th day also the rate of cell growth was higher in the case of F4 and therefore it can be inferred from it that this scaffold shows best-suited characteristics for wound healing potential. Fig.4.1.12 shows the metabolic activity of the cells over the scaffolds.

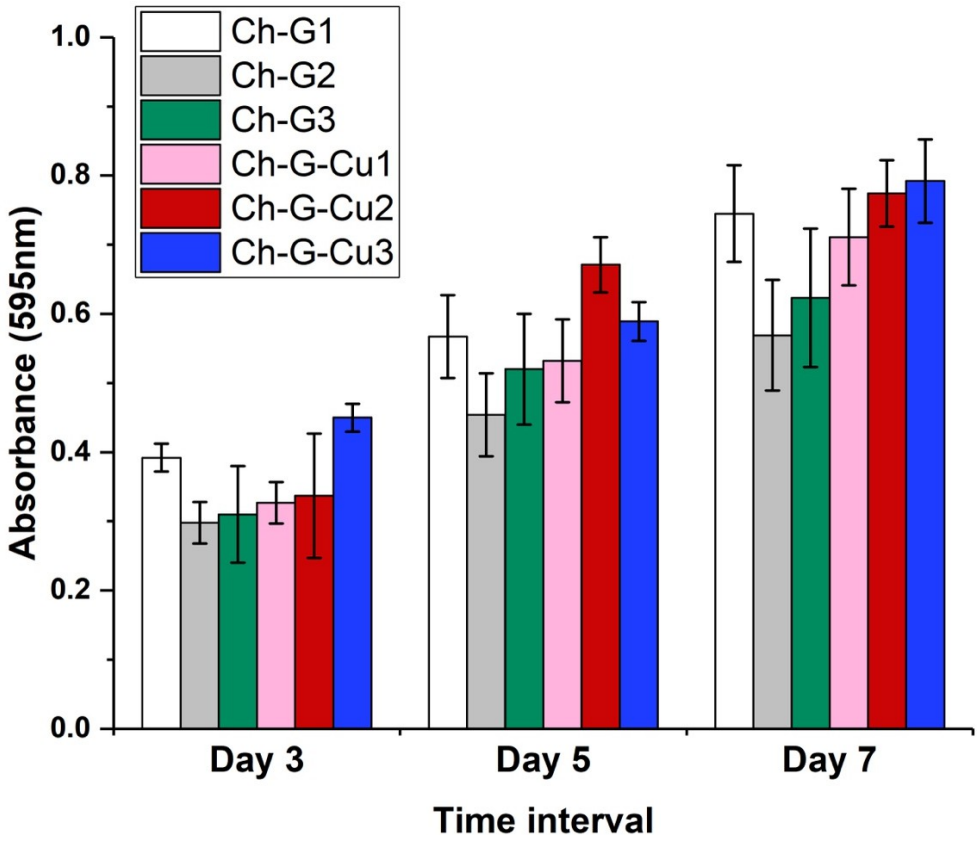

Figure 4.1.12: MTT assay of L979 cell-line over developed scaffolds with and without CN

Microscopic evaluation of cell-seeded scaffolds

Microscopic visualization was done for the cell-seeded scaffolds and the images were taken after 7 days of incubation. Microscopy helped to obtain higher-resolution optical images in the 3D scaffolds and thereby determined the colonization of skin cells over the scaffold. Live and dead cells were visible in the fluorescence microscopy. As shown in Fig.4.1.13 (g, h, i, j, k, l) the presence of live cells in green colour has occurred all across the scaffolds. This green colour represents the live cells present over the scaffolds after 7 days of incubation.

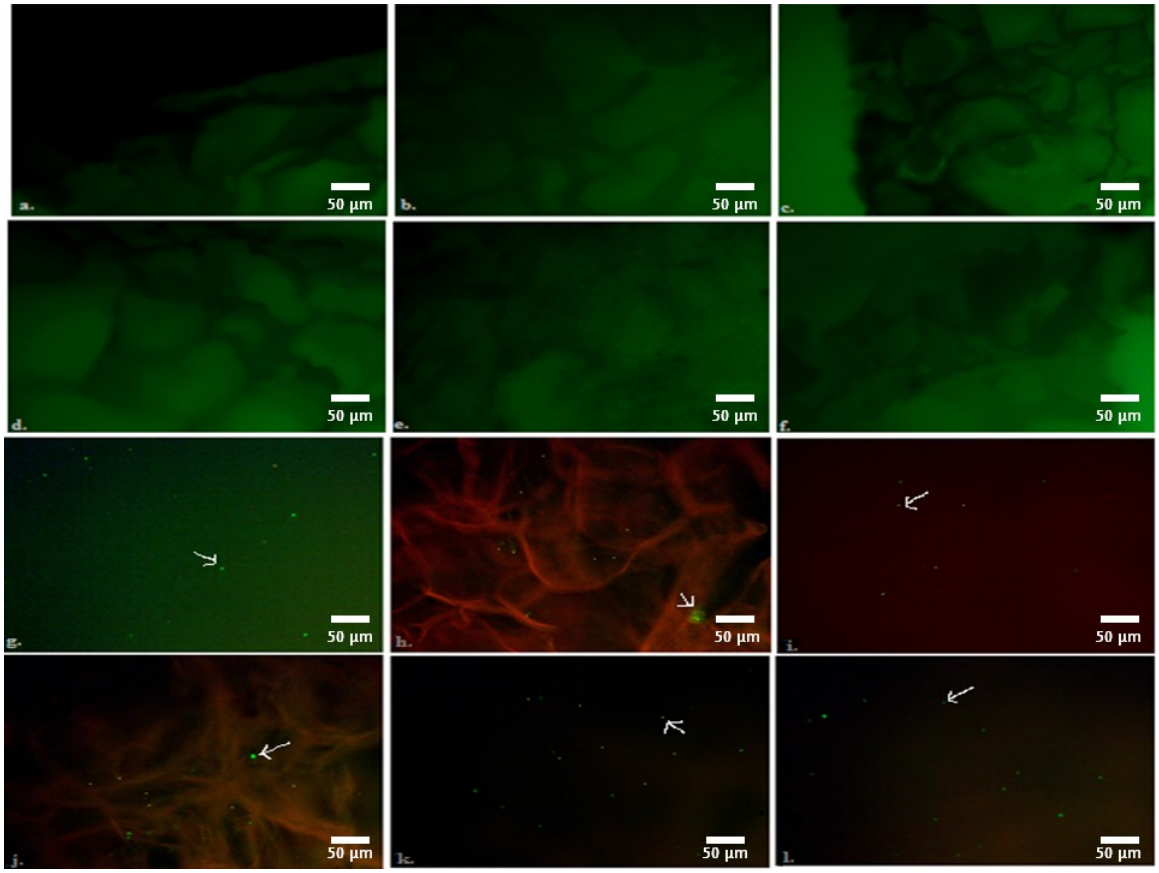

Figure 4.1.13: Microscopic images of cells seeded scaffolds with and without CN

Cell attachment study

The micrographs showed the presence of the cells attached to the scaffold surfaces. Cell growth on the scaffolds was seen in the SEM images after seeding the cells over the control scaffolds and scaffolds having copper nanoparticles. Fig.4.1.14 shows the morphological changes in the adherent cells after seeding them into the scaffolds. The analysis was done after an incubation period of 7 days the layer of fibroblast cells can be seen uniformly distributed over the scaffold's surface. In Fig. 4.1.14(e) and (f) we can see the layer that has filled in the pores of the scaffold thereby proving the effectiveness of copper nanoparticles in cell growth and proliferation.

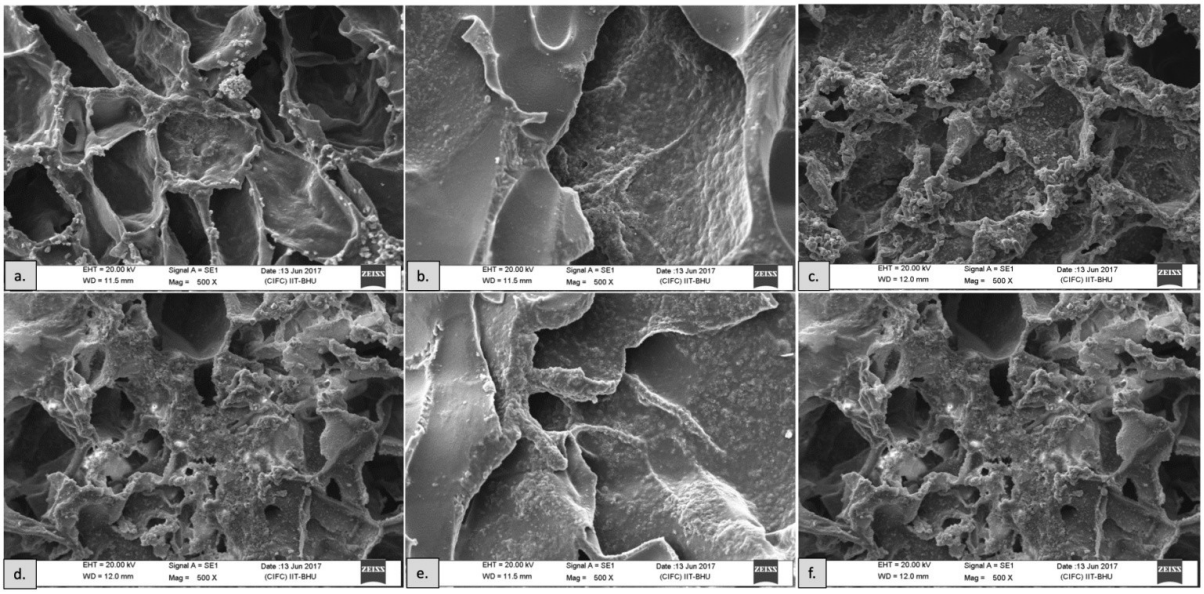

Figure 4.1.14((a-c): SEM micrographs of cell-seeded Ch-G scaffolds without CN.
Fig.4.1.14(d-f): SEM micrographs of cell-seeded Ch-G scaffolds with 0.01CN, 0.02CN and 0.03CN respectively.

Chapter 4.2

Development and Evaluation of Copper Nanoparticles and nHAP embedded Chitosan /Gelatin Nano-biocomposite Scaffolds

4.1. Results and Discussion

In continuation to the previous work on copper nanoparticles-based chitosan/gelatin composite scaffolds, we have further explored its application for bone tissue engineering applications due to the high mechanical strength obtained in our last work. This research study deals with the development of copper nanoparticles and nano-hydroxyapatite infused chitosan and gelatin-based nanocomposite scaffolds for bone tissue engineering applications. We have used human-origin osteoblast cells (MG-63) which were seeded over the scaffolds to investigate the novel biomimetic extracellular matrix system. Scanning Electron Microscopy (SEM) showed an average pore size between 100-146µm for all the C-G-nHAP- CN based scaffolds. The in-vitro degradation study showed 74-83% degradation for CN-based scaffolds and the degradation rate for 0.03% CN based scaffold was very close to the control scaffold with 84% degradation. Swelling ratio was highest for the Chitosan scaffold and for all the other scaffolds it was in the range between 5.25-5.93mg/mL. Compressive moduli were highest for 0.03%CN scaffold (3.32MPa) which was relatively very high in comparison to C-G-nHAP scaffold with 2.4MPa strength in a wet state. Stress train graphs also show the maximum displacement by 0.03% CN scaffold. The functional and structural analysis for the scaffolds showed the presence of nano-hydroxyapatite in the scaffold and CN peaks within the composite structure. Differential Scanning Colorimetry was also done which showed the reduced crystallinity observed in CN-based scaffolds with a T_m of 320ºC. Their 2D cell behaviour in the ECIS study showed maximum cell spreading and growth in 0.02%CN based scaffold. The cell-seeded composite was tested for MTT, ALP, DAPI and AOPI assay for testing its cytocompatibility for the osteoblast cell line. Cell proliferation was there in all the developed scaffolds including CN-based scaffolds. SEM of cell seeded scaffolds showed cell attachment and spreading in nHAP and CN based scaffolds. ALP activity was recorded highest in the case of 0.03% CN scaffold with 2.0 OD value. ARS staining was performed to support this study. From this study, it can be statistically depicted that nano-hydroxyapatite and 0.03% CN-based scaffold could be a potential biomaterial for minor to severe bone-related tissue regeneration applications.

4.2.1. Morphological, structural and functional characterization of synthesized Nanohydroxyapatite particles (nHAP)

Fig.4.2.1a shows the HRSEM image and digital image of nano-hydroxyapatite synthesized through sol-gel method. The amorphous structure of nano-hydroxyapatite (nano-HAP) is visible in Fig.4.2.1a. Fig.4.2.1b illustrates the EDAX pattern of synthesized nano-HAP which depicts the elemental composition of calcium and phosphate in nano-hydroxyapatite synthesized. The quantitative analysis of Ca:P ratio is visible by this spectrum. Fig.4.2.1c shows the Fourier Transform Infrared spectra of nano-HAP which depicts the functional groups present in the nano-hydroxyapatite. OH stretching was visible at 3568cm^{-1} and likewise for carbonyl groups peak at 1461cm^{-1} and for phosphate groups, bands at 1041cm^{-1} and 570cm^{-1} were also observed. Peak for HPO_4^- was observed at 612 cm^{-1} (Arunseshan et al.,2013). All these functional groups represent the interaction between the Ca:P deposits in the nano-hydroxyapatite synthesized. In Fig.4.2.1d, the XRD pattern of synthesized nano-HAP is visible. There are various peaks obtained in the XRD graph which shows the crystallinity of the synthesized nano-HAP. The peaks were compared with the previous literature wherein nano-HAP was synthesized using the sol-gel method (Mokhtari et al., 2019). Different crystal planes are mentioned in Fig.4.2.1d showing the exact peaks for synthesized nano-HAP.

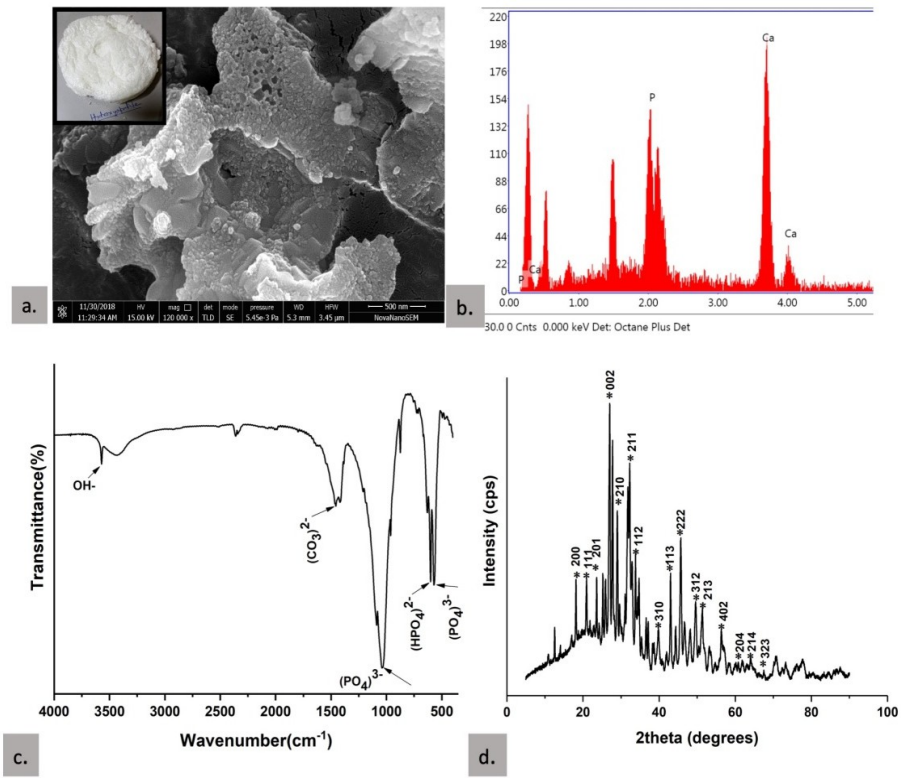

Figure 4.2.1(a): HRSEM micrograph of synthesized nano-hydroxyapatite and its physical appearance.Fig.4.2.1(b) EDAX pattern of synthesized nano-HAP. Fig.4.2.1(c)- FTIR spectrum of nano-HAP synthesized by sol-gel method. Fig.4.2.1(d)- XRD spectra of nano-HAP synthesized

4.2.2. Morphological analysis of developed scaffolds

Cylindrical-shaped scaffolds with a diameter of approximately 2cm were developed after lyophilization of the composite mixture as represented in Fig.4.2.2. The developed Chitosan-Gelatin (C-G) scaffolds were spongy and smooth over the surface and got squeezed when exerted greater pressure. After the addition of nHAP to the C-G composite solution, the structure of the scaffold turned relatively less spongy but it possessed poor strength. C-G-nHAP scaffolds possessed 150 -159 μm pore size. But with the addition of copper nanoparticles (CN), the scaffolds turned blue in colour and stiffer as represented in Fig.4.2.2(d-f). Scanning microscopic images (Fig.4.2.2) showed the porous structure of C-G- nHAP scaffolds and C-G-nHAP-CN scaffolds with 0.01%, 0.02% and 0.03% copper nanoparticles. CN-based scaffolds possessed average pore sizes between 121 ± 9.2 μm to 146 ± 9.7 μm respectively which was very close to the C-G-nHAP scaffold which had 157 ± 11.2 μm pore size. While 0.03% CN scaffolds showed 100 ± 17.4 μm pore sizes. This was estimated by microscopic images from SEM using Image J software. The scaffold possessed a more compact structure after the addition of copper nanoparticles concentration thereby reducing the pore size of the biomimetic structure. It implies that with a higher concentration of CN, the pore size decreased but this decrease was insignificant when compared to all the other scaffolds' pore size range as shown in Fig.4.2.2(d-i). From previous studies it is evident that the pore size range for bone tissue scaffolds can be between 100 - 325 μm, therefore the developed scaffolds possess desired pore size values for BTE applications (Abbasi et al., 2020a).

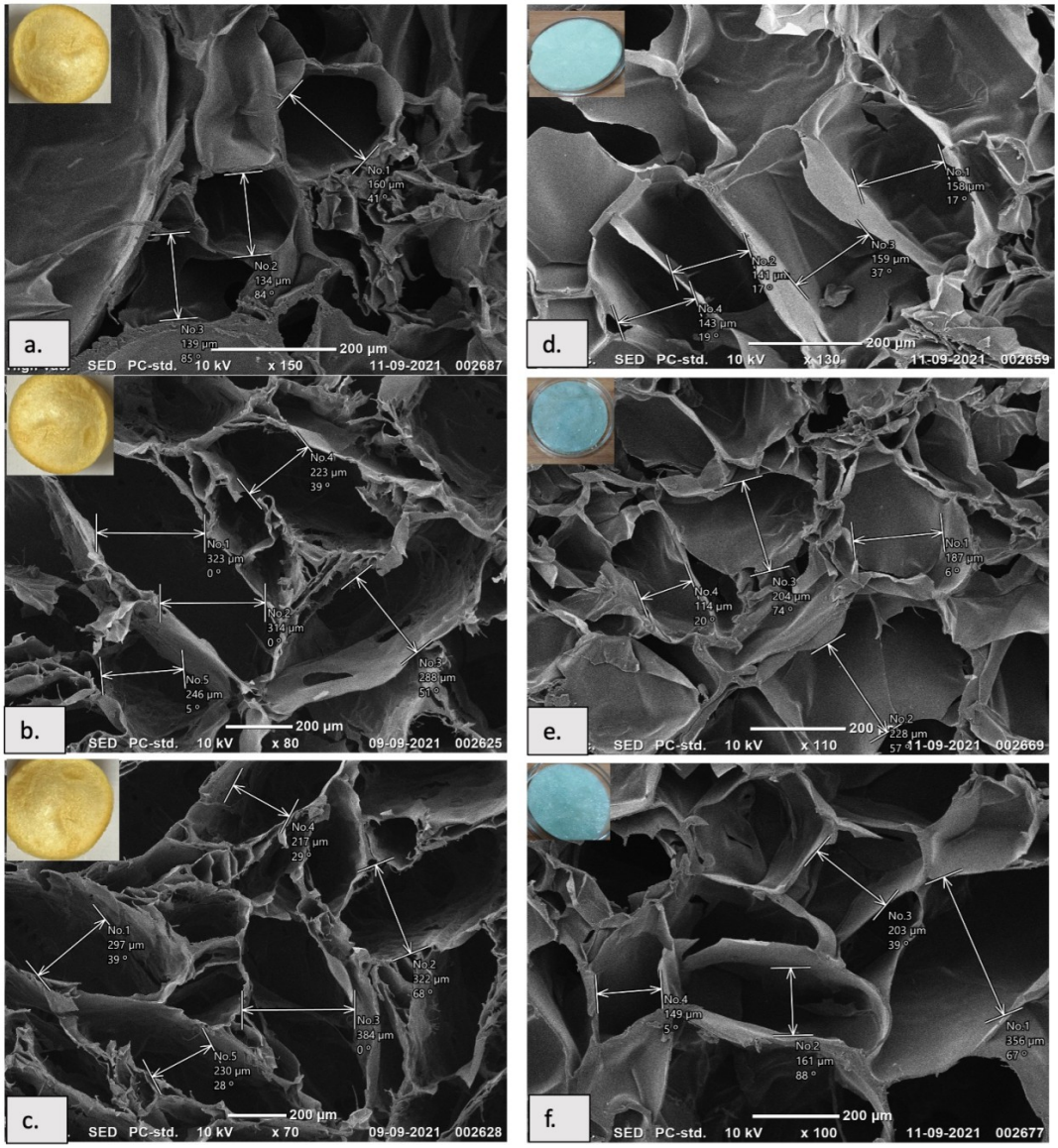

Figure 4.2.2(a-f): Digital image and SEM micrograph of developed scaffolds. Fig.4.2.2(a): SEM image of Chitosan scaffold. Fig.4.2.2(b)- SEM micrograph of chitosan gelatin composite scaffold. Fig.4.2.2(c)- SEM micrograph of nHAP incorporated chitosan-gelatin blend. Fig.4.2.2(d-f)- SEM images of Ch/G/nHAP/CN-based scaffolds with 0.01,0.02 and0.03% CN concentration.

Structural and functional analysis of the developed scaffolds

The properties of the polymer composites and blends are the result of hydrogen bonding or electrostatic interaction among the different groups. Hence, FTIR spectroscopy was done to determine the ubiquity of different functional groups that were present inside the fabricated nanocomposite scaffold. It also helps to understand the effect of copper nanoparticles on the chitosan, gelatin and nano-hydroxyapatite biocomposite scaffolds. FTIR of the developed scaffolds has been shown in Fig.4.2.3a. The major peaks were reported at 3206, 2918, 1690, 1624.12, 1551, 1265.35, 1040, 602 and 575cm^{-1}. Hydroxyl stretching of C at 3206cm^{-1} and

amide A stretched band of G at 2918cm^{-1} were analyzed due to the presence of gelatin and chitosan blend (Lewandowska et al., 2017; Pradini et al., 2018). The fading bands observed between 1560-1335cm^{-1} were due to the presence of gelatin (Konovalova et al., 2020). After the addition of copper nanoparticles, peaks were visible at 1690 cm^{-1} and 1624.12 cm^{-1} due to OH stretching. Bands between 1086-1040 cm^{-1} were predicted because of hydroxyl bonding (OH) which might be present due to chitosan gelatin and CN interaction. All three composite samples without CN consisted of similar functional groups and therefore they exhibited the common IR spectra while with the addition of copper nanoparticles these bands became weak and sharp bands were observed at around 1200-1270cm^{-1} reflecting CN interaction with chitosan and gelatin blend. Peaks between 1040-602cm^{-1} correspond to the chitosan-gelatin interaction with hydroxyapatite (Isikli et al., 2012).

Further XRD was performed for all the samples for their structural characterization. X-Ray Diffraction patterns of CN-based scaffolds and CN absent scaffolds have been shown in Fig.4.2.3b. The main peaks were observed at 16.1°, 17.7°, 21.7° and an average peak at 24.50° and 27.2°. The peak observed at 16.1° corresponds to chitosan-gelatin present inside the biocomposite. This peak started fading with the addition of copper nanoparticles as observed in Fig.4.2.3b. The amorphous property of the composite was clearly visible with the broadening peaks near 16.1°. The broad band observed near 21.7° correspond to the presence of chitosan and gelatin inside the composite (Isikli et al., 2012). The peak at 17.7° corresponds to the presence of calcium inside the composite scaffold which depicts crystallinity imparted due to the presence of hydroxyapatite (L. Sheikh et al., 2018). A slight disappearing peak near 52° depicts the presence of copper nanoparticles inside the composite (Kumari et al., 2019). The broad semi- crystalline peak angle shifted to 24.50° and then 27.2° and this was present in all the scaffold sample patterns depicting the presence of chitosan and gelatin in all the composites (Kumar P. et al., 2017).

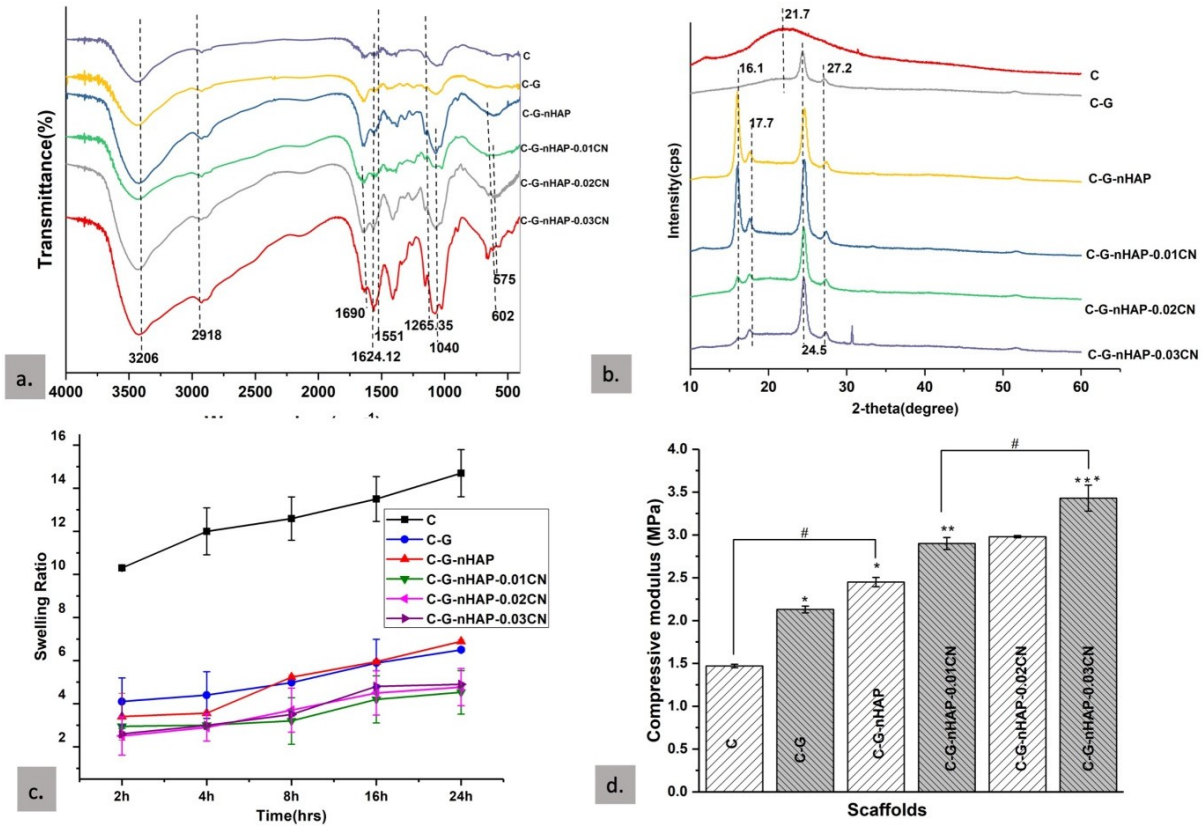

*Figure 4.2.3(a): FTIR spectra for developed scaffolds with and without copper nanoparticles. Fig.4.2.3(b)- XRD spectra for developed scaffolds. Fig.4.2.3(c)- Graphical representation for Swelling capacity of developed scaffolds.Fig.4.2.3(d)- Compressive strength for developed scaffolds. Experiments were performed in triplicates for both swelling and compressive strength evaluation including controls. The data represents the mean± standard deviation of all three experiments and the statistical difference between the different types of scaffolds is expressed by *p <0.05; **p <0.01; ***p<0.001; #p<0.0001*

Thermal stability of developed biomaterials

Differential scanning colorimetric analysis was performed for the CN-based scaffolds and without CN scaffolds as illustrated in Fig.4.2.4. Tg for all the developed scaffolds was between 50-60°C and it was not affected after the incorporation of copper nanoparticles or nano-hydroxyapatite into the samples as observed in Fig.4.2.4. However, it was observed that after the addition of nano-hydroxyapatite into the composite the melting temperature (Tm) for the samples increased to 250°C and it was almost similar for 0.01CN and 0.02CN based scaffolds also. However, for the 0.03CN-based scaffold, the melting temperature (320°C) was the highest. Hence, it can be said that with increasing concentration of CN, the melting temperature was enhanced for the scaffolds. The crystallization temperature reduced to almost 100°C after the addition of nHAP and it was similar for CN incorporated scaffolds also. But recrystallization occurred for the samples as seen in the graph. For C-G-nHAP scaffold, an exothermic step trend was observed at 300°C with an enthalpy of 72.23 J g^{-1} whereas, for C-

G-nHAP-0.01CN, there was an exothermic upside step trend observed at 100°C and then again at 280°C with an enthalpy of 61.12 J g^{-1}. For 0.02CN scaffold, an exothermic step trend was seen at 100°C and then at 275°C with almost similar enthalpy as 0.01CN scaffold. For 0.03CN based scaffold, an exothermic step trend was visible around a similar temperature and same enthalpy as for 0.02CN but it was not very peculiar therefore it can be deduced from this study that after incorporation of CN into the scaffolds, their exothermic upside step trend at 275-280°C was reduced with lower enthalpy of 61.12 J g^{-1} when compared to control scaffold. It was also observed that the melting temperature for CN based scaffolds after recrystallization was also similar in 0.01, 0.02 and 0.03CN based scaffolds (320°C). It shows that after the incorporation of n-HAP the crystallinity of the scaffolds improved and it was very close in all the scaffolds after CN addition to the scaffolds with reduced enthalpy. It can be inferred from this study that due to the higher crystallinity of the scaffolds; the MG-63 cell attachment and proliferation will also be promoted (Lee et al., 2004; Lim et al., 2005). From previous literature, it was observed that no previous study reports the thermal stability analysis for CN-based scaffolds for bone tissue engineering.

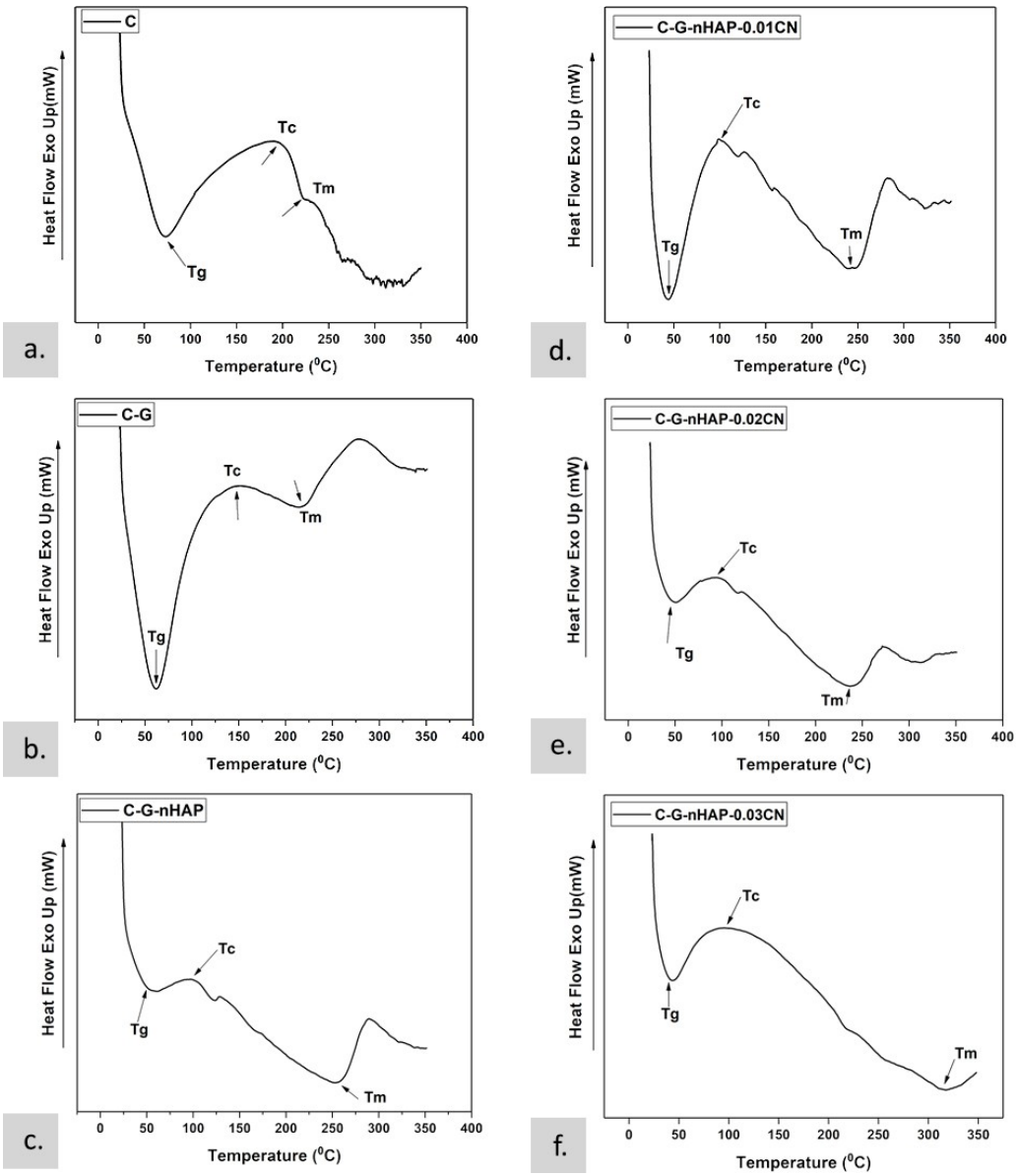

Figure 4.2.4(a): DSC graph of Chitosan scaffold. Fig.4.2.4(b)-DSC graph of C-G scaffold. Fig.4.2.4(c)-DSC graph for C- G-nHAP scaffold. Fig.4.2.4(d)-DSC graph for 0.01CN based scaffold. Fig.4.2.4(e)-DSC graph for 0.02CN based scaffold.
Fig.4.2.4(f)- DSC graph for 0.03CN based scaffold

Porosity evaluation of fabricated biomaterials

The Chitosan scaffold showed 90.12 % porosity and the C-G scaffold showed 89% porosity which was very close to the chitosan scaffold. However, it was seen that after the incorporation of nHAP in the CG composite, the porosity suddenly dropped to 86.20% porosity as shown in Fig.4.2.5a. Whereas when copper nanoparticles were added to this C-G-nHAP composite, the porosity estimated was between 80.23% to 85.20%. The porosity was 85.20% for C-G- nHAP-0.01% scaffold, 83.12% for 0.02% CN scaffold and 82.23% for 0.01% CN scaffold as seen in Fig.4.2.5a. It was evident that with the incorporation of copper nanoparticles, the porosity

decreased. But the addition of nano-hydroxyapatite into the scaffolds also led to a decrease in the porosity. It has been observed in past studies that due to the inorganic nature of nano-HAP, it gets attached to the pore surfaces which leads to a decrease in the pore sizes thus reducing the porosity (Maji & Dasgupta, 2014). But from previous literature, it is also seen that the higher value of porosity is considered significant for better infiltration of cells and nutrients (Qu et al., 2017). In our study the porosity was above 80% therefore it can be suitable for bone-related applications because a porosity of more than 60% is found to be suitable for osteogenesis (Abbasi et al., 2020b). Hence, the developed scaffolds possess good porosity which is compatible with treating bone tissue defects (Singh et al., 2019).

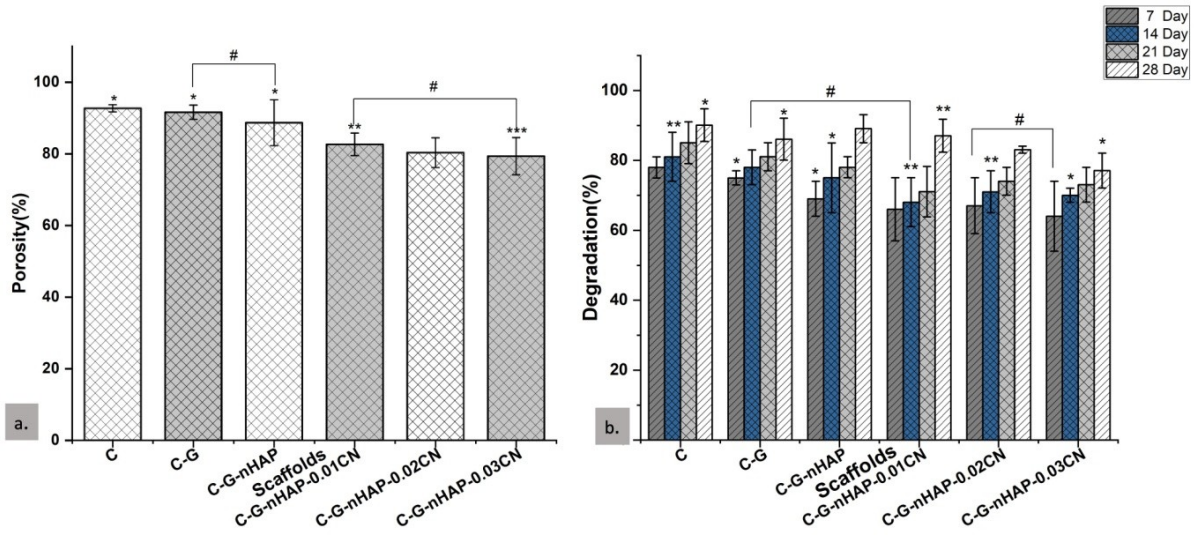

*Figure 4.2.5(a): Graphical representation of Porosity of fabricated scaffolds. Fig.4.2.5(b)- In-vitro degradation study for developed scaffolds for 28 days. The data are represented as mean ± standard deviation obtained from three different experiments performed in triplicates. Statistical analysis was performed by ANOVA analysis of variance followed by Tukey's test wherein *p <0.05, **p<0.01, ***p<0.001, #p<0.0001*

Water retention capacity of developed scaffolds

Fig.4.2.3c shows the water uptake ratio of C, C-G, C-G-nHAP scaffolds and C-G-nHAP-CN scaffolds. Water uptake by scaffolds suggests cell infiltration, and adequate nutrient supply, hence it may promote cell adhesion and cell migration. The results suggested that the water uptake ratio of CN-based scaffolds lies in the range of 5.25-5.93mg/mL. While in the case of positive control C-G-nHAP scaffold the water uptake ratio was in a similar range as for CN-based scaffolds. But for CG-based scaffold, it was the highest between 13.53 to 14.12mg/mL which could be due to the hydrophilic nature of chitosan and gelatin. The swelling behaviour of the scaffolds changed on the augmentation of CN and nano-hydroxyapatite gradually after some time which could be because of the addition of crystalline nanoparticles into it. The

continuous downfall in the swelling was observed after a few hours which implies that a constant increase in the concentration of CN and hydroxyapatite nanoparticles affects the

Water retention capacity of developed scaffolds

Fig.4.2.3c shows the water uptake ratio of C, C-G, C-G-nHAP scaffolds and C-G-nHAP-CN scaffolds. Water uptake by scaffolds suggests cell infiltration, and adequate nutrient supply, hence it may promote cell adhesion and cell migration. The results suggested that the water uptake ratio of CN-based scaffolds lies in the range of 5.25-5.93mg/mL. While in the case of positive control C-G-nHAP scaffold the water uptake ratio was in a similar range as for CN-based scaffolds. But for CG-based scaffold, it was the highest between 13.53 to 14.12mg/mL which could be due to the hydrophilic nature of chitosan and gelatin. The swelling behaviour of the scaffolds changed on the augmentation of CN and nano-hydroxyapatite gradually after some time which could be because of the addition of crystalline nanoparticles into it. The continuous downfall in the swelling was observed after a few hours which implies that a constant increase in the concentration of CN and hydroxyapatite nanoparticles affects the overall surface chemistry of the scaffolds which limits their ability to absorb more fluid after a certain time duration. Yet the 0.01CN and 0.02CN incorporated scaffolds whose swelling ratio is 5.93mg/mL can be useful for bone regeneration clinical applications as suggested by previous studies (Peter M. et al., 2010). This finding has not been reported previously, hence, it can be a major aspect of CN-incorporated scaffolds for researchers to further study its application for bone tissue-related applications.

Mechanical strength evaluation of scaffolds

The mechanical properties of the scaffold play important role in neo bone tissue regeneration. Scaffold must have desired mechanical properties that facilitate osteogenic differentiation of cells over the scaffold. The mechanical properties such as compressive strength and compressive strain at break of the prepared cross-linked scaffold was measured using UTM machine. Mechanical testing of the scaffolds was performed to analyze the suitability of the samples for bone regeneration as shown in Fig.4.2.6d. The compressive strength for C and C-G scaffolds was between 1.4MPa to 2.2MPa which was much less for bone regeneration applications. However, as soon as nano-HAP was added to scaffolds, the strength and stability of the scaffold improved. As we know the maximum load-bearing capacity reflects the compressive strength of any scaffold therefore for each scaffold the load-bearing capacity was measured using the stress- strain graph. However, the compressive strength for the C-G-nHAP

scaffold was 8MPa which served as a control for other CN-based scaffolds (Maji et al.,2016). The C-G-nHAP scaffold load-bearing capacity was 8kN as shown in the Fig.4.2.6(a) after which it showed a decline in the load-bearing capacity. The mechanical strength was enhanced tremendously with an increased concentration of copper nanoparticles in C-G- nHAP-CN scaffolds. We saw that after the addition of 0.01%CN into the scaffolds the load-bearing capacity reached to 10MPa and similarly for 0.02% CN, it was 14MPa after which the scaffold showed increased displacement. While for 0.03%CN scaffold, the load-bearing capacity increased to a maximum of 16MPA. It was visible in the results that after the augmentation of CN in the scaffolds, the mechanical strength improved significantly to almost 70%. It is also seen from a previous study that CN nanoparticles enhance the compressive modulus to almost 82% which is very prominent (Shuai et al., 2020). Hence these CN-based scaffolds might be suitable for further studies on Bone tissue engineering. Although 0.03% CN-based scaffold possessed the highest compressive strength but the texture was more brittle therefore it can be inferred that we could not apply it for BTE applications.

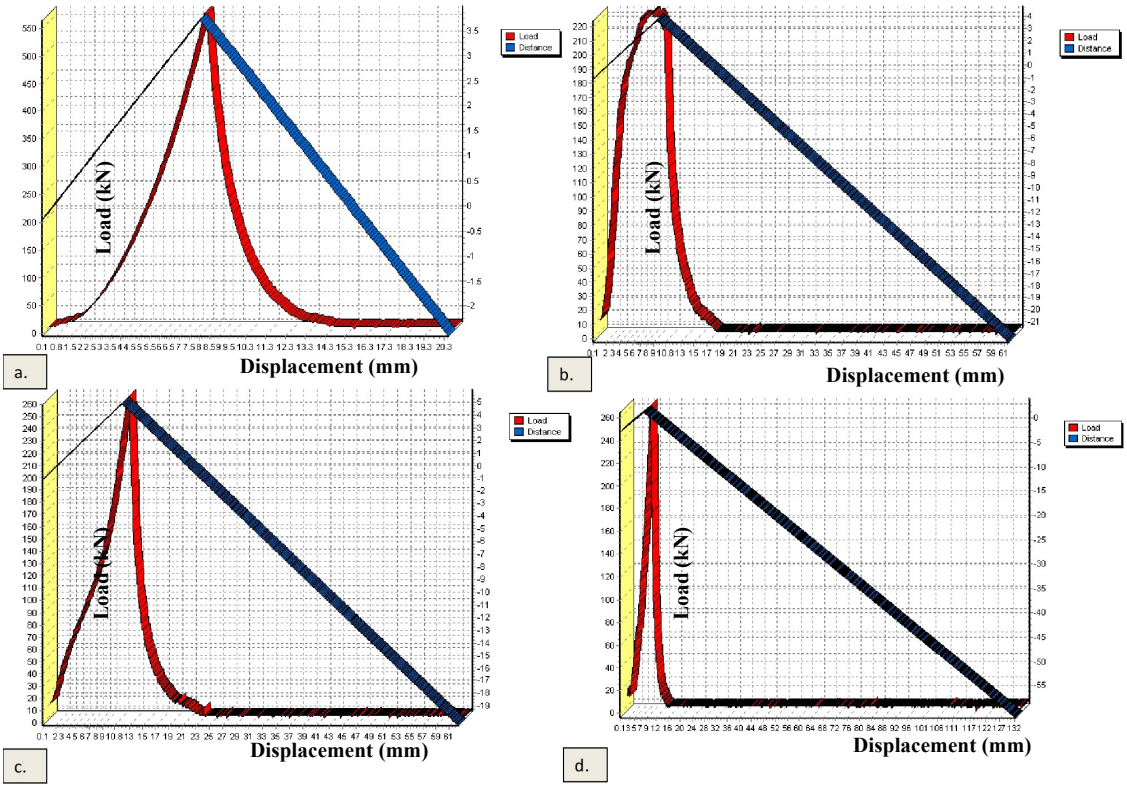

Figure 4.2.6(a): Stress-strain plot for positive control C-G-nHAP scaffold. Fig.4.2.6(b-d)- Stress-strain curve for all the CN-based scaffolds with 0.01, 0.02 and 0.03 CN nanoparticles composition respectively.

In-vitro degradation analysis of developed scaffolds

Fig.4.2.5b shows the biodegradation of C, C-G and C-G-nHAP scaffolds and C-G-nHAP-CN based scaffolds. It was observed that there was a pattern observed in the degradation rate of the developed scaffolds. The degradation rate was maximum for C and CG scaffolds but it kept on decreasing after the incorporation of nano-hydroxyapatite. But the lowest degradation rate was observed in the case of 0.03%CN scaffolds with a severe loss in the structural integrity after incubation in lysozyme (104U/mL) solution. In the case of C and C-G scaffolds, the degradation rate was too high (80-90%) as observed in Fig.4.2.5b. For C-G- nHAP-0.01CN scaffold the degradation rate (83.12 ± 2.3) was very close to C-G-nHAP scaffold (positive control). However, C-G-nHAP-0.02CN scaffold possessed a lower degradation rate of 81% yet it was relatively sufficient than C-G-nHAP-0.03CN scaffolds with 74% degradation rate on the 28th day.

The degradation rate was prominently reduced in control scaffolds but if we consider the CN-based scaffolds it was seen that with a higher concentration of CN nanoparticles, the degradation rate reduced tremendously after 21 days. This reduction might be due to the mechanical property of copper nanoparticles which enhanced the overall mechanical strength of the scaffold. Yet if we compare it with chitosan scaffolds, there was a major weight loss in it. From previous studies, it is clear that a reduced degradation rate must also be suitable for bone tissue regeneration which not only supports cellular growth and proliferation but also results in better cell attachment (Alsberg et al., 2003; Amini et al., 2012b). It was also observed that the scaffolds developed in this study possessed a better degradation rate than previous studies on bone regeneration (Alsberg et al., 2003; Fu et al., 2010). From this study, it can be concluded that even after the incorporation of 0.03% CN into the scaffolds, the degradation rate was clinically sufficient for the biomaterial to get degraded within the due course of time along with promoting bone regeneration at the defect site.

ECIS study

The electric cell impedance sensor measured the impedance (Z) and the capacitance (C) of the cells. The impedance measurement was performed between the two 81E gold electrodes for 45h over a 4000Hz frequency. Fig.4.2.7c illustrates the change in impedance with time at 4000Hz frequency. It can be implied from this graph that the change in the impedance was due to the growth of MG-63 cells. It can be observed in Fig.4.2.7c that the cell growth pattern was similar for all the cases including the C-G-nHAP scaffold except 0.02%CN scaffold. In the case of the 0.02%CN scaffold, the cell growth deceleration occurred very soon. This might be due to the surface of the scaffold which couldn’t provide a uniform structure for cell adherence.

Fig.4.2.7a represents the graphical representation of resistance generated by the cells at 4000Hz frequency. The continuous growth and death of MG-63 cells with hourly change were observed in this graph. The total resistance was calculated using the Equation 5.

$R_{total} = R_1 + R_2 + R_3$----------Eq.5

It shows that the highest cell growth was observed between 30-40h and it was maximum for 0.01% CN scaffold. This was not the case for the 0.02% CN scaffold wherein the resistance dropped and was sturdy till 42h. From the overall study, it can be concluded that the maximum cell growth was observed in the case of 0.01% CN scaffold and it was lowest in 0.02% CN scaffold. This observation is also supported by a plot of overall capacitance vs time as shown in Fig.4.2.7b. It shows how the impedance increased and the capacitance decreased when the MG-63 cells attached rapidly to the surface of the electrode (Siddiquei et al., 2010). The total capacitance was calculated using Equation 6.

$1/C_{total} = 1/C_1 + 1/C_2 + 1/C_3$ ----------Eq.6

It also corresponds to the increase in the number of cells that enhance the total resistance since every single cell contributes to a small resistance. It was also seen that after 40 h, the cell growth declined and the attachment rate to the 81E electrode surface was also reduced and saturated.

The impedance analyzer provides measurements of both the impedance (Z) and the phase angle (Θ). Impedance measurements between the two gold electrodes were taken at six-hour intervals over a wide frequency range from 0.5 Hz to 15 MHz. Fig. 4.2.7 illustrates the change in impedance measurements (Z) over this frequency range. Two measurements are illustrated in this figure, namely the impedance of the cells after 6 h and 54 h of incubation respectively. It can be concluded that the change in impedance was due to the growth of MG-63 cells. The noise in the impedance is produced by the magnetic stirrer inside to incubator. The impedance analyzer provides measurements of both the impedance (Z) and the phase angle (Θ).

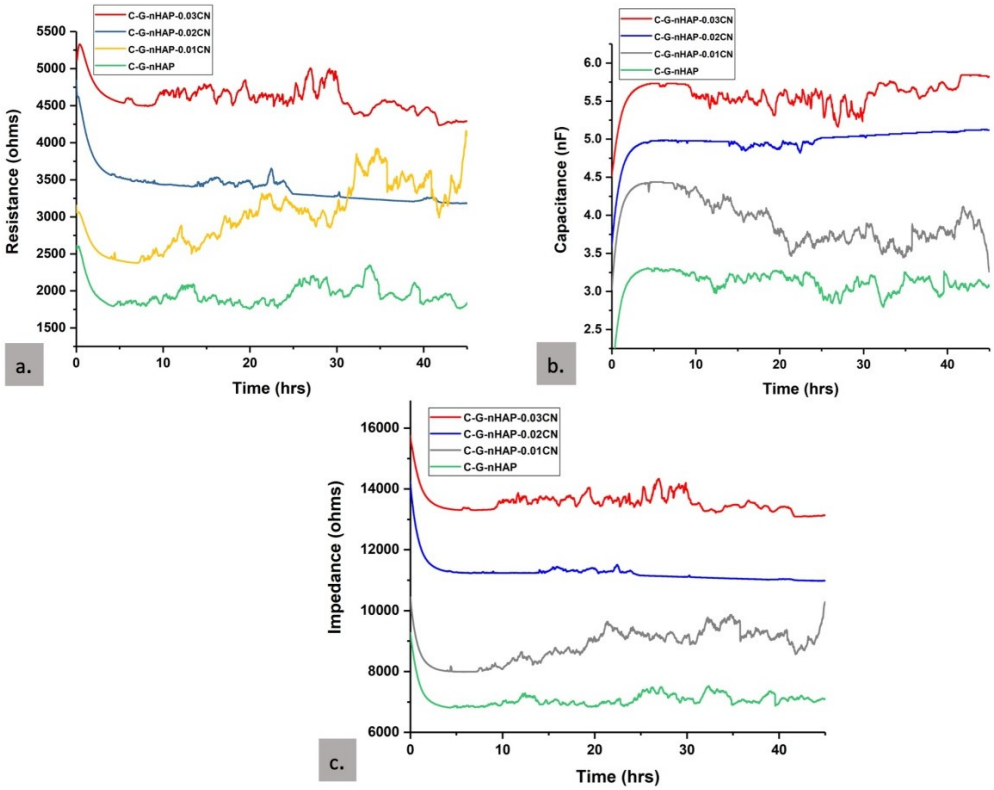

Figure 4.2.7(a): Resistance generated by cells spread over the 2d array. Fig.4.2.7(b)-Capacitance measurement of the osteoblast cells developed over scaffolds on the 2D array. Fig.4.2.7(c)- Impedance graph for MG-63 cells cultured over the scaffolds for 45 h.

Cell cytocompatibility evaluation

Nuclear staining with DAPI showed that MG-63 cells were healthy and firmly attached to the scaffolds. They were mostly round and spindle in shape. Fig.4.2.8 shows the bright field images and fluorescent images of the MG-63 cells over the developed scaffolds on the 3rd day of cell culture. DAPI-stained cells and AOPI-stained cells are shown in Fig.4.2.8. It was also evident that after the incorporation of nanohydroxyapatite, the scaffolds demonstrated enhanced cellular response, and improved cell attachment and proliferation were also observed on day 3. The cell spreading distribution enhanced after the incorporation of nanohydroxyapatite and it was uniform across the developed biomaterial. From previous studies, it is clear that nanohydroxyapatite addition enhances the mechanical strength of the scaffold in combination with other polymers (Kashiwazaki et al., 2009). Therefore, even after the addition of CN into scaffolds, the cell viability was satisfying in comparison to the positive controls i.e., the C-G-nHAP scaffold. This might be due to the mechanical strength imparted by CN and nHAP and the RGD residues of gelatin present over the scaffold's surface. The results showed that mostly MG-63 cells remained over the surface of the scaffold and they maintained their specific osteoblast-like morphology even after the incorporation of CN into the scaffolds. However, it

is evident from the image that 0.01% CN scaffolds showed the maximum proliferation among others, and 0.03% CN-based scaffold showed cytotoxicity of cells visible on the surface of the scaffold. Therefore, from this study, we can infer that 0.01% CN incorporated scaffold can be beneficial for bone tissue engineering applications.

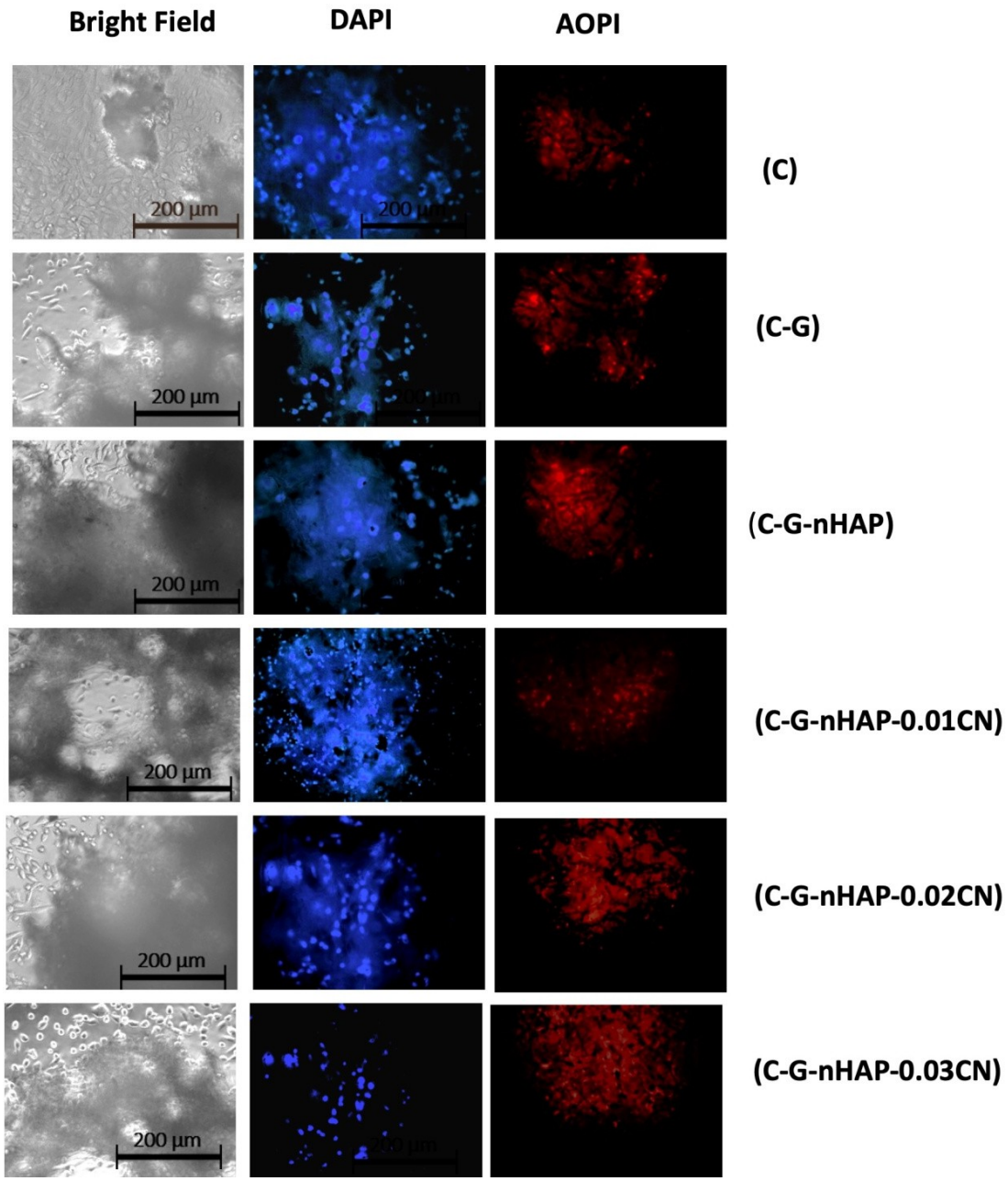

Figure 4.2.8: Bright field, DAPI and AOPI microscopic images of osteoblast cells on 7th day of culture

MTT assay

Since cell metabolic activity is considered an important parameter while studying the cytocompatibility of a scaffold. Cell growth profiles of MG-63 cells cultured over C-G-nHAP

scaffold and CN-incorporated scaffolds (C-G-nHAP-CN) are shown clearly in Fig.4.2.9a. MTT assay was done for 3 days, 7 days and consequent 14 days keeping media treated surface without scaffold as the positive control for it. The cellular growth of MG-63 cells was promoted after CN addition in the scaffolds. As seen in Fig.4.2.9a, the cell viability was highest in the case of 0.03%CN-based scaffold and it increased continuously with increasing days when compared to the positive control and 0.01%CN and 0.02% CN scaffolds. From one of our previous studies performed over CN-based scaffolds, it was concluded that the 0.03% CN-based scaffolds were not good for cell attachment or growth but in this study, we achieved a higher growth rate for bone cells (Kumari et al., 2019). Thus, proving its efficacy for bone tissue regeneration applications. It can also be due to the properties of copper nanoparticles and nano-hydroxyapatite applied in the scaffold development which also enhanced the mechanical strength thereby improving the osteogenic environment for the cells. Therefore, 0.03CN-based scaffolds are the most suitable candidate for bone regeneration applications.

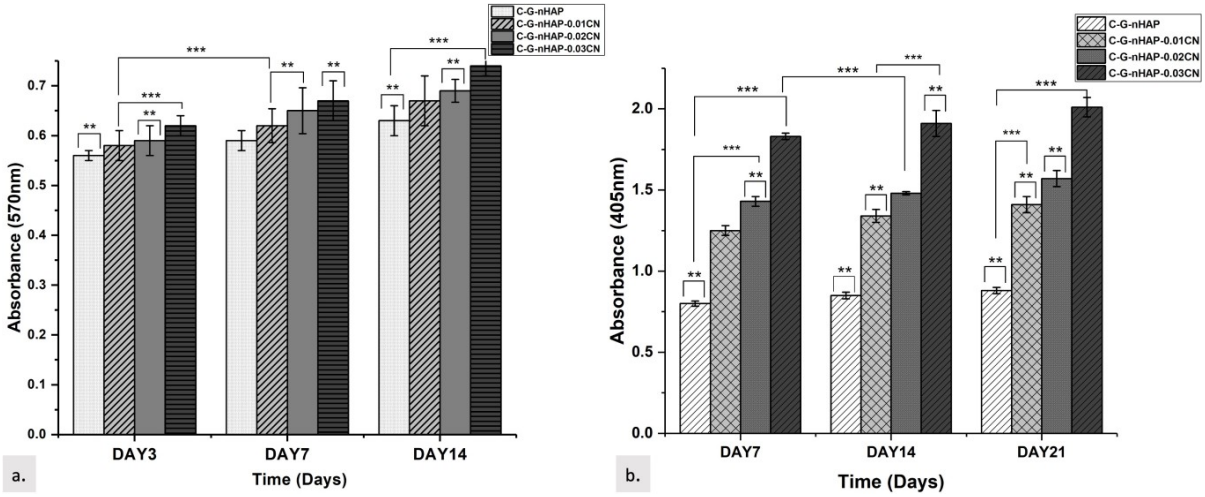

*Figure 4.2.9a-MTT assay of osteoblast cells over fabricated scaffolds for 3,7 and 14 days. Fig.4.2.9b- ALP activity of osteoblast cells over developed scaffolds for 21 days. All the experiments were performed in triplicates and the data sets are represented as mean ± standard deviation. The significance study was conducted using ANOVA analysis and Tukey's test wherein *p<0.05, **p<0.01, ***p<0.001*

Alkaline phosphatase (ALP) activity expressed by MG-63 cells

Fig.4.2.9b represents Alkaline phosphatase expression for all the CN-based scaffolds and C-G-nHAP scaffold for 21 days incubation period. Alkaline phosphatase expression was enhanced gradually for MG-63 cells that were cultured on C-G-nHAP-CN scaffolds with respect to different incubation time intervals. For C-G-nHAP scaffold, the ALP activity increased with increasing time duration and this might be due to the biocompatible nature of polymers and nano-HAP which itself is a mineral component of bone extracellular matrix. But

after the incorporation of CN into scaffolds, there was a magnificent rise in the ALP activity that was observed specifically on day 21. The osteogenic expression was highest in the case of C-G-nHAP-0.03%CN scaffold, signifying that the cells illustrated maximum differentiation behaviour on day 21 rather than those on days 7 and 14. Moreover, osteoblasts that were cultured on the C-G-nHAP scaffold showed one-fold activity escalation on the 21st day. While copper nanoparticles on the other hand induced better cell differentiation as observed in previous studies (Shuai et al., 2020). The 0.03CN-based scaffold showed a radically elevated ALP activity in contrast to C-G-nHAP scaffolds on the 14th day and 21st day. This might be due to the degradation products of the scaffolds which form the main constituents of bone matrix (calcium and phosphate) and also the intrinsic properties of copper nanoparticles which promoted the cellular differentiation of MG-63 cells. Overall, MG-63 cells cultured over 0.3%CN-based scaffolds showed maximum osteoblast differentiation activity in comparison to other scaffolds. Therefore, it can be a promising candidate for bone regeneration applications.

SEM of MG-63 cells seeded over developed scaffolds

The SEM micrographs show the cell adhesion and spreading over the scaffold's surface. The cellular network of MG-63 cells is visible in all the scaffolds, they were capable of better adherence and spreading after the incorporation of nanoparticles that include nano-HAP and CN. The SEM micrographs in Fig.4.2.10 demonstrate the circular morphological osteoblast cell colonies over the scaffold's surface (Venkatesan et al.,2014). The cell spreading of MG-63 cells was improved in comparison to control in the case of CN based scaffolds. It was evident from these images that the higher surface area and rough surface of the scaffolds provided by nano-HAP and CN incorporation provided a better platform for the proliferation of the MG-63 cells. The aggregation of cells in Fig.4.2.10b suggests that nano-hydroxyapatite was responsible for the improved cell adhesion. The protruding structure on the scaffold shows the cells that attached to the fibrous network of scaffold slowly. Fig.4.2.10c, d and e demonstrated the cellular morphology of MG-63 cells and depicted the enhanced cell spreading which suggests that CN combination with nano-HAP and chitosan and gelatin might be a suitable choice for bone bioengineering applications (Mahmoodi et al.,2011).

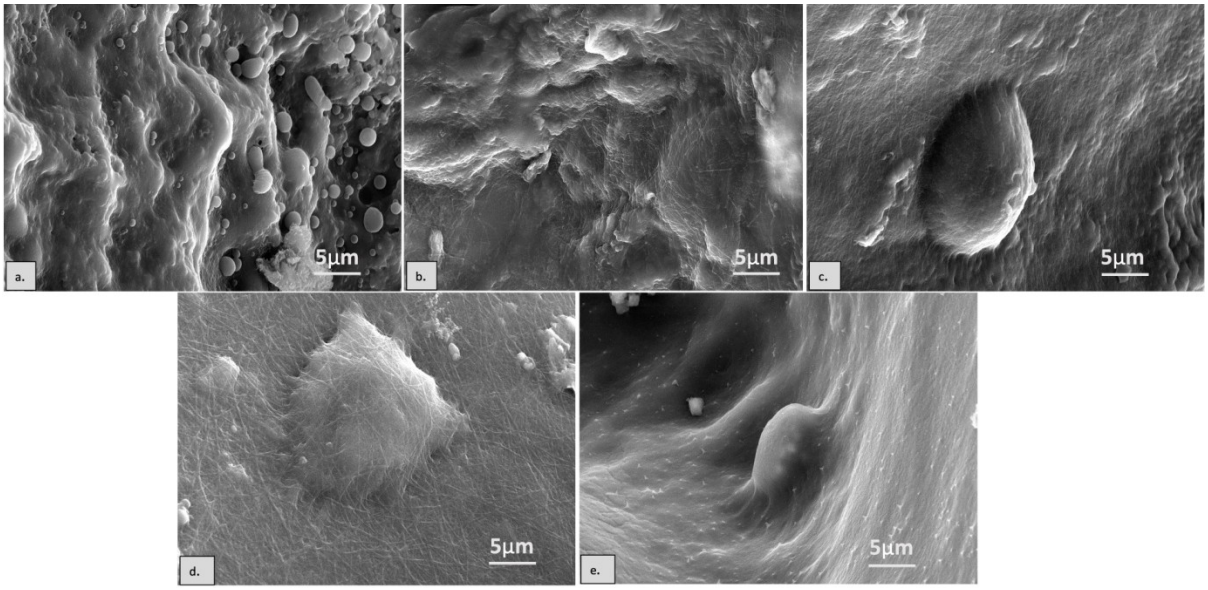

Figure 4.2.10- SEM micrographs of cell-seeded scaffolds after 7 days of culturing; a. C-G, b. C-G-nHAP, c. C-G-nHAP-0.01CN, d. C-G-nHAP-0.02CN, e. C-G-nHAP-0.03CN

Alizarin red assay of MG-63 cells

Fig.4.2.11a and b show the alizarin red staining of MG-63 cells over developed scaffolds. It shows that after the 14th day of culture, a considerably higher amount of mineral deposition was observed in the case of C-G-nHAP-0.01CN and C-G-nHAP- 0.03CN based scaffold when compared to the control. But it was surprising to see that C-G-nHAP-0.02CN based scaffold showed relatively lesser mineralization on day 14. The microscopic images of the cultured scaffolds in Fig.4.2.11b do not show any red-coloured mineral nodules formed on the overall 3D structure due to reduced osteogenic differentiation. It can be inferred from this that the samples might have been harvested earlier before the proper deposition of calcium ions which resulted into such a result. However, from previous studies, it has been observed that nanohydroxyapatite presence greatly impacts the mineralization process as reported in previous studies (Pepla et al., 2014). Therefore, the proper time shall be given to the scaffolds for calcium deposition for ARS staining to examine the calcium deposition occurring. The combination of CN into the composite promotes the biomineralization process as evident from the image. Fig.4.2.12 represents the graphical representation of ARS-stained cells.

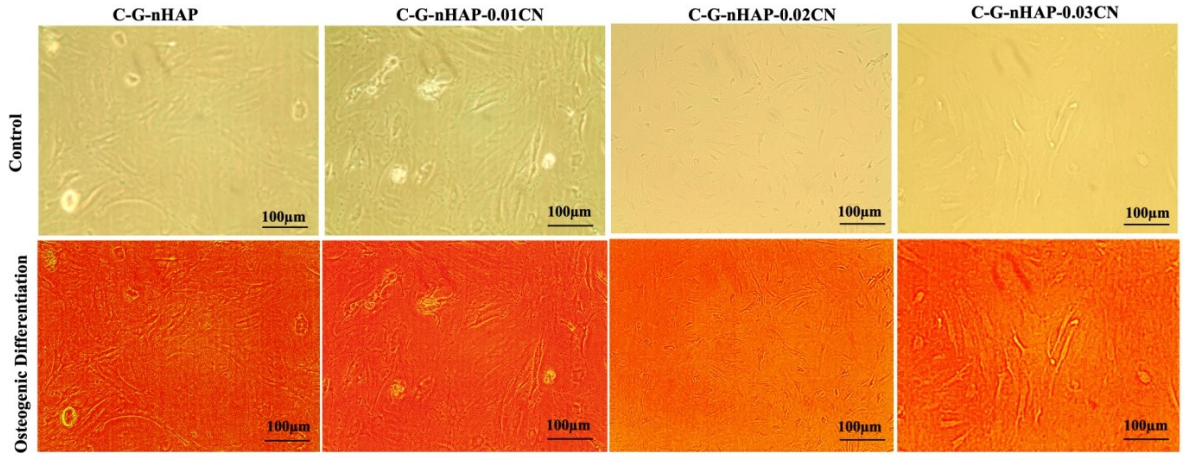

Figure 4.2.11- Alizarin red staining of all the developed scaffolds on day 7 as control and osteogenic differentiation on day 14.

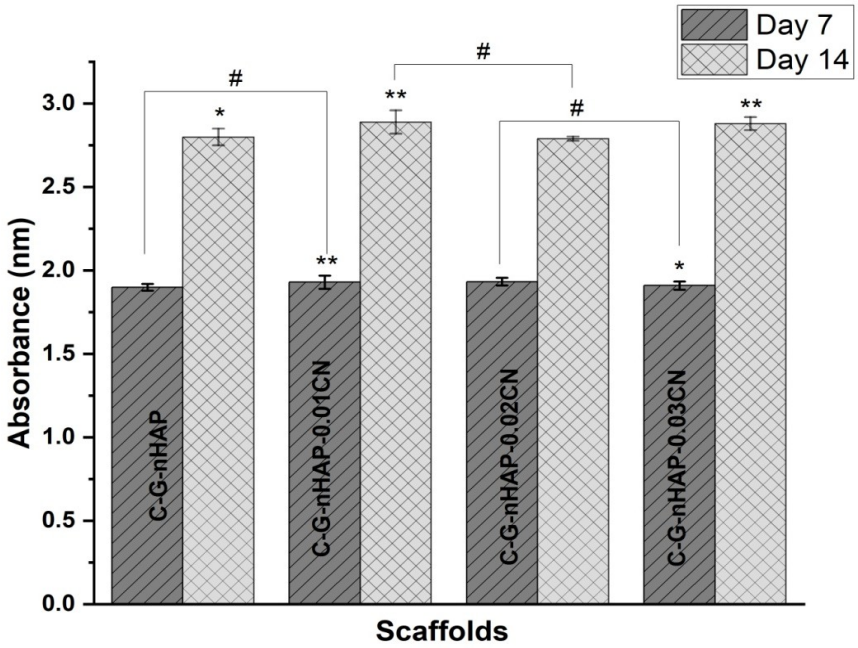

*Figure 4.2.12- Graphical representation showing the mineralization occurring on day 14 depicting the osteogenic differentiation of MG-63 cells over the developed scaffolds. All the experiments were conducted in triplicates. Every data set is represented as mean ± standard deviation for the individual experiments. The significance analysis was performed by ANOVA analysis and then Tukey's test: *p<0.05, **p<0.01, #p<0.0001*

Chapter 4.3

Development and Evaluation of Chitosan/Gelatin based scaffold modified with Tri-calcium phosphate/Nano-bioglass for Bone Tissue engineering applications

4.1. Results and Discussion

In the previous chapter, we successfully developed a higher mechanical strength scaffold of chitosan/gelatin by incorporating n-HAP and CN yet we wanted to attain a scaffold with enhanced porosity and mechanical strength of between 0.1 to 30MPa mimicking human trabecular bone. As we have discussed earlier nanobioglass has shown good improvements in porosity and mechanical strength. Therefore, in this study as a novel approach, we develop chitosan and gelatin-based artificial biomimetic 3D structures that are crosslinked with EDC-NHS/glutaraldehyde solution and then loaded with freshly synthesized nanobioglass (NBG) and Beta Tri-calcium phosphate (ß- TCP) in three different ratios (1:0,0:1 and 1:1) respectively. It is performed to develop a potential artificial acellular bone graft for load-bearing bones. Ch/G blends have proven to be efficacious for bone tissue regeneration as reported in previous chapters due to their biocompatibility, hydrophilicity, wound healing properties and osteogenic properties. Nanobioglass is adopted in this study due to its bioactivity, osteoconductive nature and higher mechanical strength (Bhisham et al.,2020; Maji et al.,2016). Whereas ß- TCP is used in this research because previous studies have shown that calcium phosphate like HAP has been used widely for formulating ECM mimicking the natural bone and ß- TCP is also one of the sources of calcium phosphate for bone (Zhao et al.,2006). Few studies that were done on ß- TCP have shown that it has a ten times higher degradation rate than HAP and it was used in several composites for attaining higher compressive strength than regular chitosan/gelatin scaffolds and HAP scaffolds (Detsch et al.,2008). However, ß- TCP shows good mechanical strength with Ch/G blends as reported in previous studies (Serra et al.,2015; Yin et al.,2003). But it still needs to have a cohesive understanding of the structural and functional relationship with NBG and therefore in this phase of work, we aim to develop a scaffold with improved mechanical strength using different ratios of NBG and ß- TCP without compromising the osteoconductivity and biodegradability of scaffolds. The prepared scaffolds are also characterized for morphology, structural, functional, physicochemical properties and bioactivity. This present research study describes the above experiment's results and discussion.

4.3.1. Characterization of Nanobioglass Synthesized

In this study, we have utilized nanobioglass that was freshly synthesized in the laboratory and was incorporated into the nanocomposite scaffolds therefore HRSEM, XRD and TEM analysis was done for its characterization. Since the crystalline nature of bioglass is very essential for the structural properties and biological behaviours of developed scaffolds. Therefore, a typical HRSEM micrograph, digital image of NBG, TEM micrograph, its SAED pattern and XRD spectra of NBG are given in Fig.4.3.1a, b, c and d respectively. Fig.4.3.1a shows the photographic image and HRSEM micrograph of synthesized nanobioglass. The agglomerated shape of synthesized nanoparticles is visible in Fig.4.3.1a which might have happened due to the sample preparation for HRSEM. Therefore we conducted further characterization analysis to confirm that the synthesized nanoparticles exhibit the properties of nanobioglass. The TEM micrograph in Fig.4.3.1c and Fig.4.3.1e shows the size of the spherical-shaped nanoparticles of bioglass in the range of 200nm scale as reported by Lukowiak and his team using the same procedure for nanobioglass synthesis. (Lukowiak et al.,2013). Whereas, XRD spectra of NBG in Fig.4.3.1b illustrate the characteristic peak of NBG at 2theta=24 degrees which depicts the crystalline form of the nanobioglass prepared. Fig.4.3.1d represents the TEM diffraction pattern of synthesized nanobioglass.

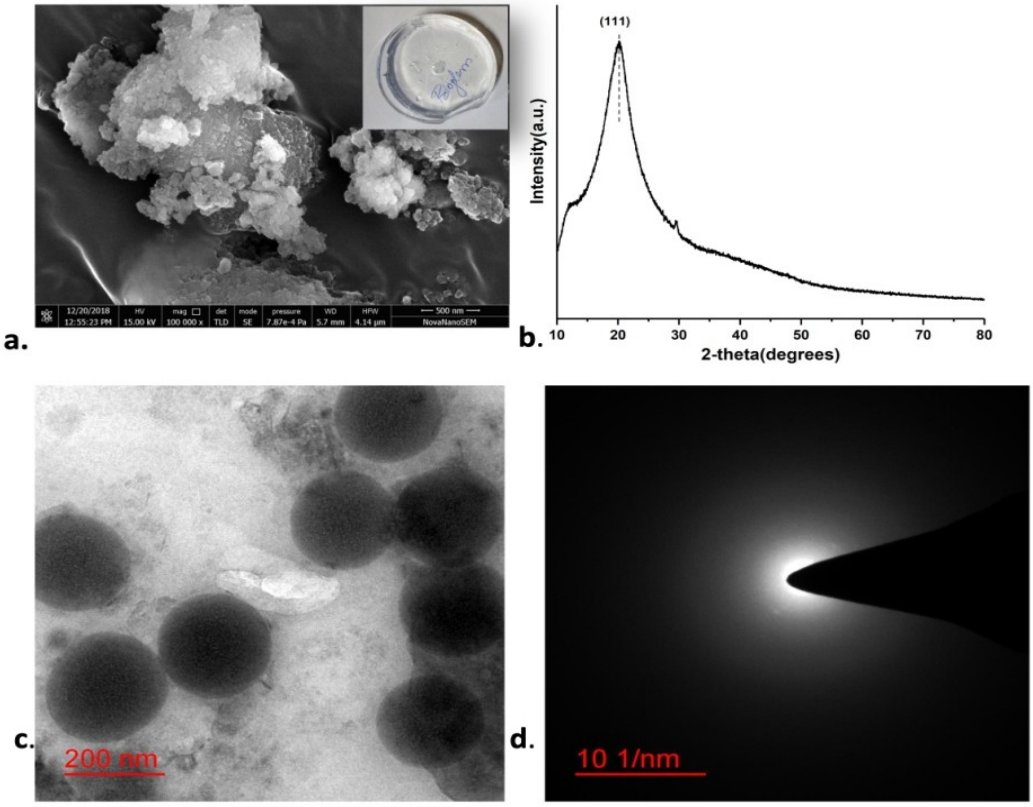

Figure 4.3.1(a): Photographic image of nanobioglass and HRSEM image of freshly prepared Nanobioglass. Fig.4.3.1(b)- XRD spectra of NBG synthesized Fig.4.3.1(c-d)- TEM image and SAED pattern of developed NBG.

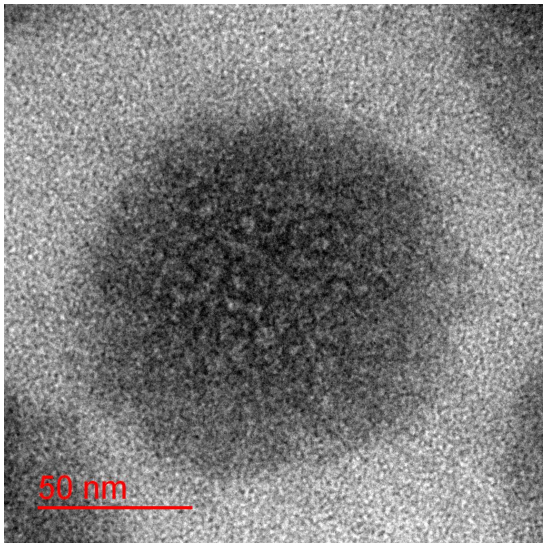

Figure 4.3.1(e): TEM image of the synthesized nanobioglass using sol-gel method

4.3.2. Characterization of Scaffolds

Physical and Morphological characterization of developed scaffolds

Fig.4.3.2 shows the digital image of the developed scaffolds and also their high-resolution SEM micrographs at 500µm and 200µm scales. The HRSEM micrographs represent the porous interconnected microstructures of the fabricated scaffolds with the novel crosslinking method. It can be observed that the scaffolds developed were beige in colour in the digital images. The average pore size of the developed scaffolds was between 220 µm to 265 µm and literature suggests that porous structure between 100 µm - 200 µm is effective for osteoblast cell growth but they prefer larger pore size (Abbasi et al., 2020). The scaffolds possess enhanced pore size therefore it suggests that the prepared scaffolds might be suitable for osteoblast cell growth and regeneration of mineralized bone after implantation.

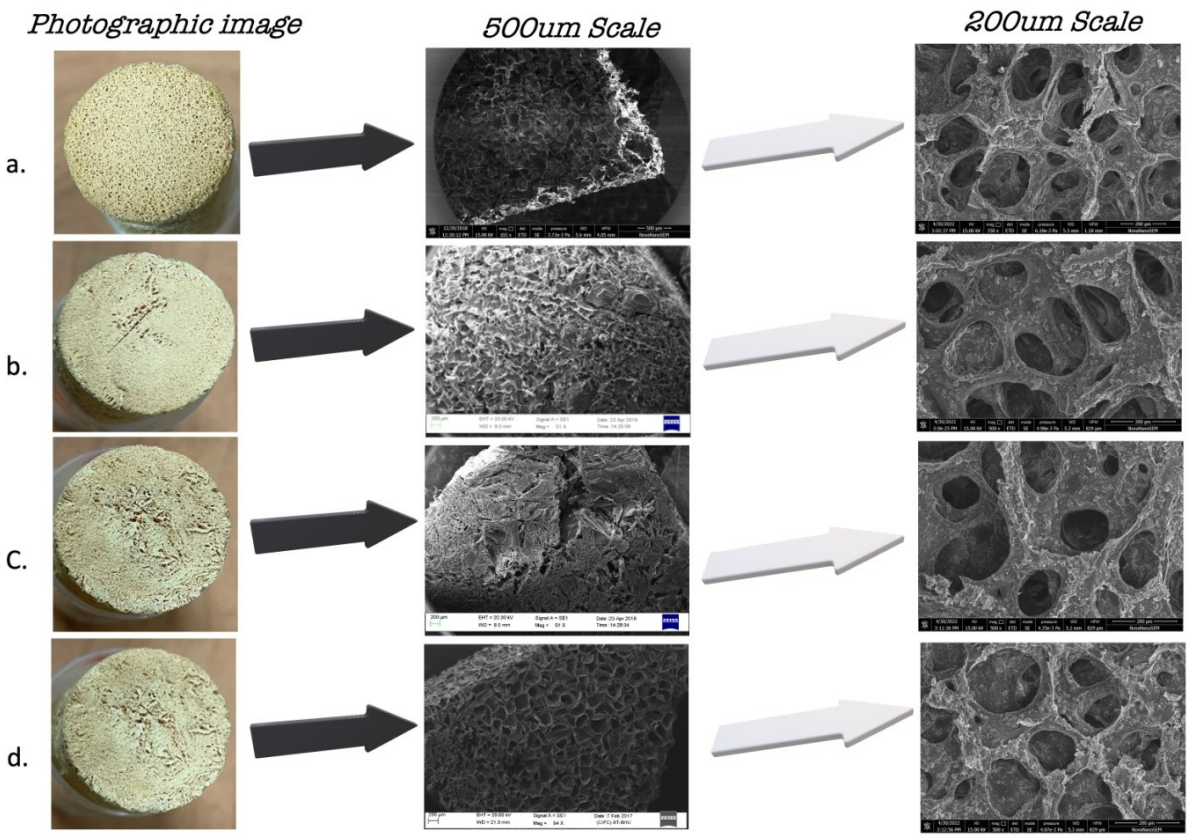

Figure 4.3.2(a): Ch-G scaffold and its HRSEM images at 200 and 500µm scales. Fig.4.3.2(b)- Ch-G-NBG scaffolds with HRSEM images. Fig.4.3.2(c)-Ch-G-TCP scaffold with HRSEM images. Fig.4.3.2(d)-Ch-G-NBG/TCP scaffolds with HRSEM images at 200 and 500µm scale.

Structural and functional characterization of developed scaffolds

FTIR spectra of the scaffolds were performed as shown in Fig.4.3.3a. Since chitosan and gelatin both share common functional groups. It shows the characteristics band formed at around 3350 cm^{-1} and 2922 cm^{-1} which corresponds to O-H stretching and C-H stretching respectively that occurs due to chitosan-gelatin interaction (Samimi Gharaie et al., 2018). The bands observed at 1660 cm^{-1} depict the Amide-I bonding due to the presence of nanobioglass (Maji et al., 2016b). Then the peak at 1119 cm^{-1} and 553 cm^{-1} corresponds to β-tri-calcium phosphate. Peaks at 1552 and 1655 cm^{-1} correspond to imine C-N which might have formed due to the crosslinking of the scaffolds with EDC-NHS and glutaraldehyde solution (Yin et al., 2003). To assess the crystallinity of developed scaffolds after nanobioglass and ß-TCP incorporation, XRD was performed as shown in Fig.4.3.3b. It depicts that the characteristic peaks of chitosan and gelatin both were suppressed by the huge broad amorphous peak due to the incorporation of nanobioglass between 20-40 degrees. However, it was observed that after the addition of ß-TCP into the scaffolds, the crystallinity suddenly enhanced for the scaffold samples. The characteristic peaks at 17.5, 24.6, 27.2 and 30.5 degrees correspond to the crystalline nature imparted due to ß-

TCP. These peaks are attributed to crystal planes of 110, 024, 214 and 0210 that are related to ß-tricalcium phosphate (Choi & Kumta, 2007).

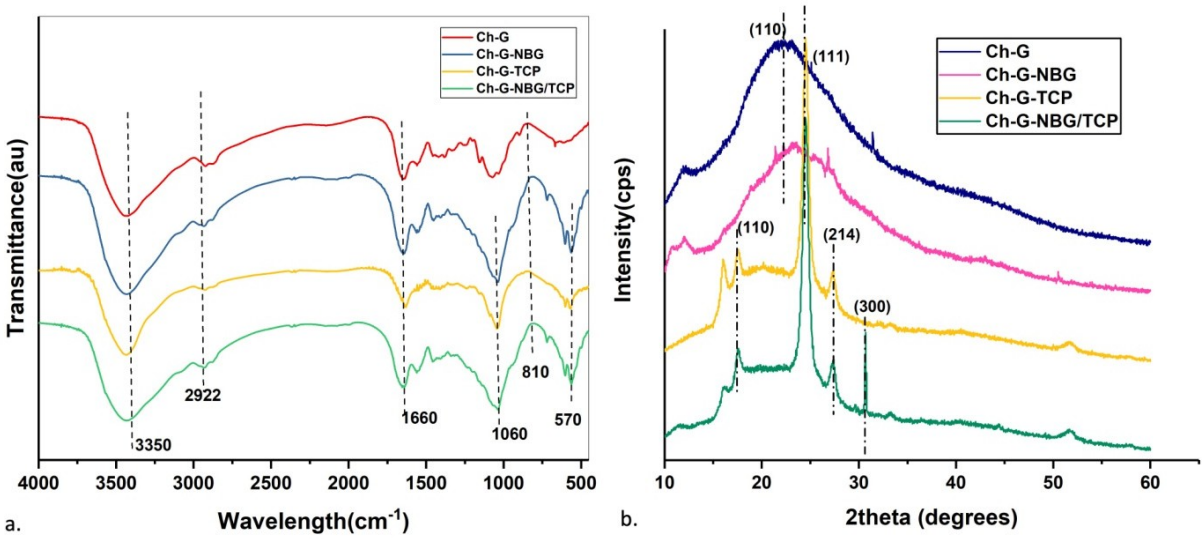

Figure 4.3.3(a): FTIR spectra of all the fabricated scaffolds including control.
Fig.4.3.3(b)- XRD spectra of developed scaffolds

Porosity estimation for fabricated scaffolds

In this study, the porosity was calculated using Liquid Displacement Method. In Fig.4.3.4 it is evident that the crosslinked scaffolds formed are highly porous with large interconnected pore sizes. As can be seen in Fig.4.3.4 Ch-G-NBG scaffolds possess larger pore sizes than Ch-G-TCP and the pore size is 265.2 ± 11.41µm which is neither very high nor low. It is sufficient for bone cells to grow and proliferate over it. We can also observe the uniform distribution of ß-TCP and NBG inside the pore walls of the scaffolds which gently reduced the average pore size in the case of TCP/NBG scaffolds to 215.1 ± 9.12 µm. However, the pore size got reduced after crosslinking, and the porosity was still maintained by the developed scaffolds. Previous studies showed that pore size between 215.1 ± 9.12 µm to 265.2 ± 11.41µm is better when compared to previous research for bone tissue engineering (Serra et al., 2015). Therefore, in the liquid displacement method, the porosity for all the crosslinked scaffolds came out to be >80 ± 1.3(S. Wu et al., 2014b). This established the fact that porosity was maintained in all the scaffolds even after the addition of crystalline materials and this was not affected even after the EDC-NHS /Glutaraldehyde crosslinking. Overall, the achieved porosity is suitable for bone tissue engineering applications.

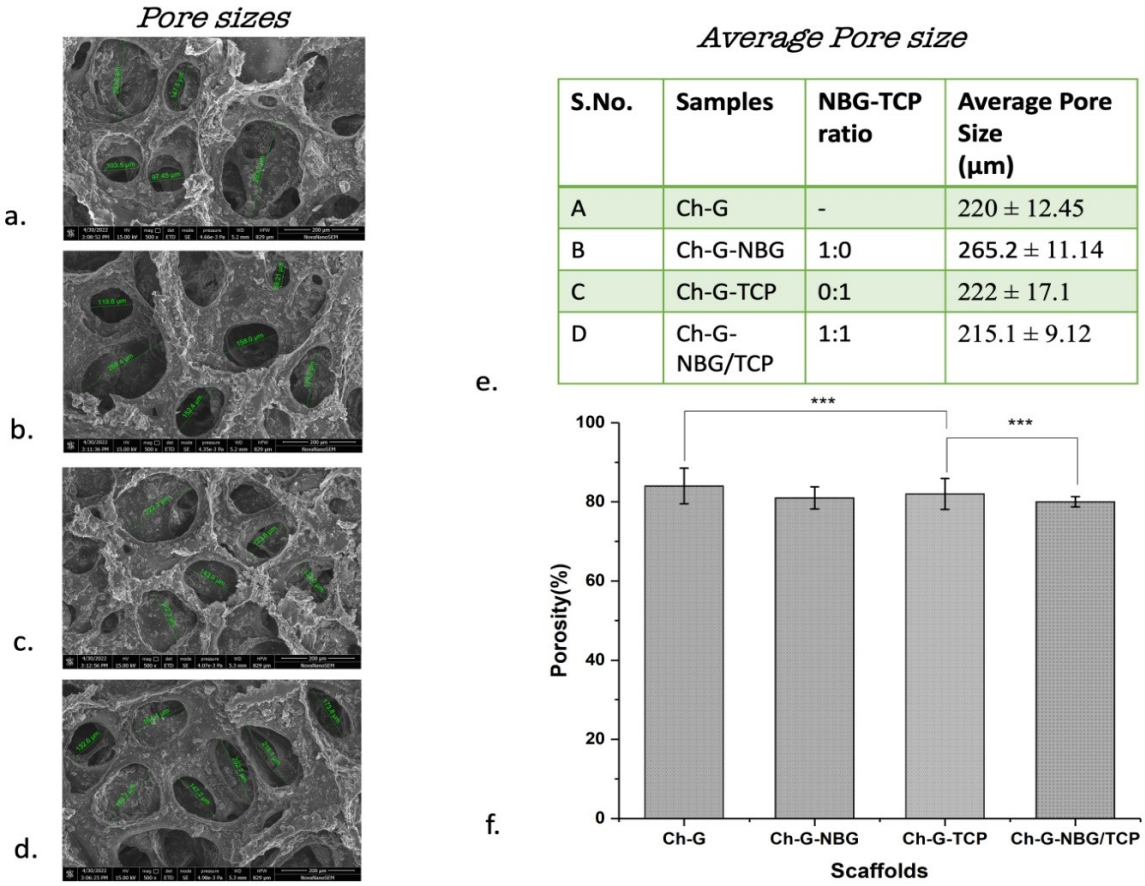

S.No.	Samples	NBG-TCP ratio	Average Pore Size (µm)
A	Ch-G	-	220 ± 12.45
B	Ch-G-NBG	1:0	265.2 ± 11.14
C	Ch-G-TCP	0:1	222 ± 17.1
D	Ch-G-NBG/TCP	1:1	215.1 ± 9.12

*Figure 4.3.4: It represents the different pore sizes for all the developed scaffolds (a)Ch-G. (b)Ch-G-NBG, (c)Ch-G-TCP and (d)Ch-G-NBG/TCP respectively. Fig.4.3.4(e)- Tabular representation of average pore size for developed scaffolds estimated through image J software using the HRSEM images. Fig.4.3.4(f)- Graphical representation of Porosity of developed scaffolds through liquid displacement method. Experiments were performed in triplicates and the data is represented as mean± standard deviation for the experiments. The statistical difference between the scaffolds of different types is expressed as ***p<0.05.*

Swelling capacity of the fabricated scaffolds

The developed scaffolds can easily swell up in the water due to the presence of hydrophilic gelatin and chitosan polymers. Swelling capacity influences the expansion of the pores which leads to better cellular infiltration and nutrient exchange. Hence swelling possesses an essential role in TE but exceeded swelling of the scaffold might lead to a loss in mechanical strength of the scaffolds. Therefore, it is essential to maintain an optimum swelling profile for the developed scaffolds.

The scaffolds started swelling up as soon as we placed them in the PBS solution. But it slowly reduced after 30-40mins. By this, we assume that when these scaffolds will be implanted inside the body, they will swell up rapidly by the action of bodily fluids and this will completely fill the remaining gaps just like in the micro 3D environment (Zolghadri et al., 2019). Fig.4.3.5b shows the swelling ratio and the weight gained due to the swelling of the scaffolds. The

swelling ratio of Ch-G scaffolds was significantly higher than that of Ch-G- TCP, TCP/NBG scaffolds and Ch-G-NBG scaffolds. This could be due to the reduced surface area as the inorganic material attached over the pore walls couldn't absorb fluids, unlike polymers. This could also be due to the hydrophilic nature of polymers. But when compared to the control, the swelling ratio decreased steeply after the addition of ß-TCP and NBG into the scaffolds. This might be due to the interaction between polymeric materials and the inorganic components. Studies, where ß-TCP has been utilized for bone tissue scaffold fabrication, have shown that the swelling ratio decreased after the inorganic component incorporation, therefore, the developed scaffolds possess the effective swelling capacity for bone regeneration application (Serra et al., 2015). From previous studies, it is evident that the swelling ratio of these scaffolds appeared to be suitable for bone tissue grafts (Amini et al., 2012)

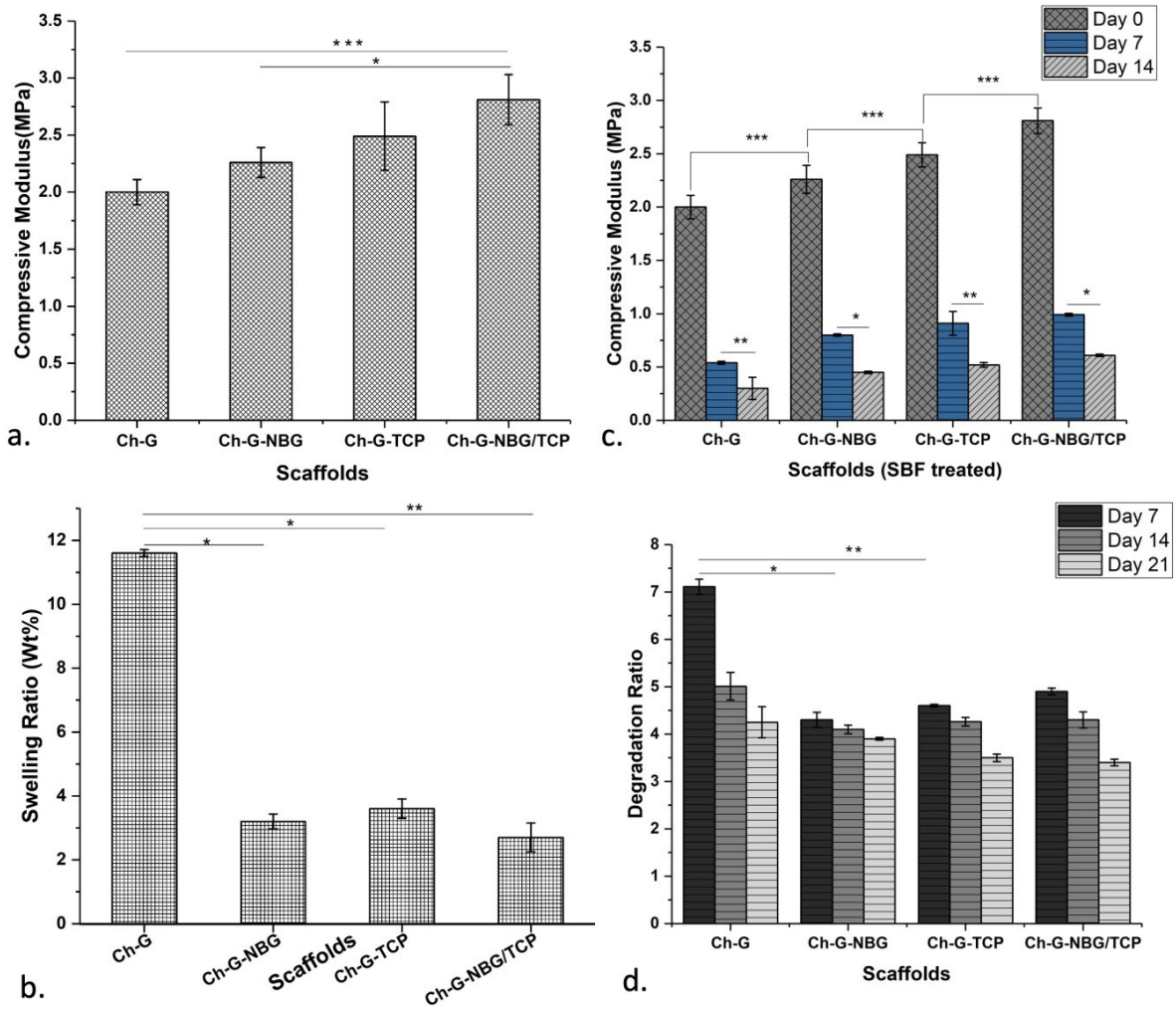

*Figure 4.3.5(a):Graphical presentation of compressive strength of developed scaffolds. Fig.4.3.5(b)- Swelling uptake study of developed scaffolds. Fig.4.3.5(c)- Graphical presentation of SBF-treated scaffolds for 0,7 and 14 days. Fig.4.3.5(d)-21 days degradation evaluation graph of the scaffolds. All the experiments were performed in triplicates and the data is represented as mean± standard deviation for the experiments. The statistical difference between the different kinds of scaffolds is expressed as *p<0.05; **p<0.01; ***p<0.001.*

Compressive strength of developed scaffolds

We assume that the ß-TCP and NBG accumulated at the walls of the pore significantly affected the mechanical strength of the scaffolds. Fig.4.3.5(a) shows the comparison in the mechanical properties of Ch-G, Ch-G-TCP, Ch-G-NBG and Ch-G-TCP/NBG scaffolds in the test. As observed there appeared to be a massive difference in the compressive moduli of these scaffolds especially, Ch-G-TCP/NBG scaffold as per two-way analysis ($n=5$, $U=0$ and $p<0.05$). Furthermore, the compressive values (CV) obtained for these scaffolds showed that the CV of Ch-G (2.1 ± 0.010 MPa) was very low than that of Ch-G-TCP/NBG (2.7 ± 0.045 MPa) scaffold as per ANOVA analysis. The notable enhancement in the compressive moduli from 2.25 ± 0.013 MPa to 2.7± 0.045 MPa suggests that this occurred due to the incorporation of ß-TCP and NBG inside the biocomposite material (Kumar et al., 2017). For Ch-G-NBG scaffold the CV was evaluated to be 2.25± 0.015 MPa which was relatively lower than Ch-G-TCP scaffold (2.5 ± 0.016 MPa) yet they both possessed higher mechanical strength than the Ch-G scaffold. In one of the previous studies, it was seen that the mechanical strength for cancellous bones can be between 20 to 200MPa and for trabecular bone, it can be between 0.22 to 10.44Mpa (Bose et al., 2012; Maji et al., 2018). Comparatively in our study, the mechanical strength for NBG/TCP scaffolds (2.7 ± 0.045 MPa) is very much in the range for bone tissue grafts and therefore they can be applied in bone bioengineering applications.

When the scaffolds were treated with SBF for different time intervals, it was observed that on day 0, the compressive value was relatively higher than on day 7 and it reduced much more on day 14. For Ch-G-NBG scaffold the CV was 0.45 ± 0113MPa and for Ch-G-TCP/NBG scaffold it was 0.6 ± 0.011MPa which was comparatively higher than the control scaffold with 0.3 ± 0.012MPa. Fig.4.3.5c shows the mechanical strength of SBF-treated scaffolds for different time durations. This was due to the incorporation of the crystalline bioceramics ß- TCP and NBG into the scaffolds. The simulated body fluid (SBF) treatment shows how the mechanical stability has improved after the addition of these components. They also lead to the formation of an apatite layer that also leads to better firmness of the scaffold due to these components (SiO_2, Ca^{2+} and PO_4^{3-}). Our study showed improved mechanical strength after SBF treatment from previous studies which showed that the addition of nanobioglass led to the enhancement of mechanical strength (Singh et al., 2019a). Thus, the compressive strength obtained for these scaffolds shows that they can be a promising tool for bone tissue engineering applications.

Evaluation of scaffolds *in-vitro* degradation

Biodegradation of the samples is shown in Fig.4.3.5d. In 21 21-day study, the samples underwent continuous degradation in the presence of lysozyme. It was observed that the control sample (Ch-G) degraded to 71.1 ± 1% which was the most among the other samples. We also observed that after the addition of NBG into the sample, the degradation reduced to 55 ± 10% which was about a 25% decrease in the degradation rate. Similarly, in Ch-G-TCP scaffold, the degradation rate was 53% ± 1.3% which was very close to Ch-G-NBG scaffold. In the case of Ch-G-NBG/TCP scaffold, it was seen that the degradation rate was 59 ± 7% which was also close to other samples. All this weight loss percentage depicts that the presence of crystalline particles in the scaffolds lowered the degradation rate. However, since the mechanical strength enhanced after the addition of crystalline biomaterials, therefore it can be predicted that it was the reason for the delay in the degradation of these samples. From Fig.4.3.5d, it is evident that the weight loss in the case of NBG and ß-TCP scaffolds was slower from day 7 to day 21. Similarly, it can be observed in Ch-G scaffolds the degradation rate was comparatively higher than in bioceramics based scaffolds. Studies suggest that the degradation rate should not be fast enough for the cells to form a layer of tissue (Zhang et al., 2014). Since our biomaterial is bioresorbable in nature due to the presence of ß-TCP and it has similar components as bone, therefore, its degradation products will help in the neo-bone formation. Some studies have shown that controlled degradation rates can also be achieved for bone tissue engineering (Feng et al., 2021; Maji et al., 2016c). Hence, the degradation percentage attained in this study is suitable for treating defects of bone tissue.

Thermal stability evaluation (DSC)

Fig.4.3.6. a, b, c and d show the thermal stability of developed scaffolds between 25 to 350°C. The melting temperature for all the scaffolds after recrystallization was in a similar range (300-325°C). For Ch-G-TCP and Ch-G-NBG/TCP scaffold, an exothermic step trend was observed at around 300°C with an enthalpy of 170.21 J g^{-1} and 164.13 J g^{-1} respectively. For Ch-G and Ch-G-NBG scaffolds exothermic step trend was observed at 270°C with an enthalpy of 168.78 J g^{-1} and 169.92 J g^{-1} respectively, which was almost similar. It showed how after the incorporation of the bioceramics components into the scaffolds, the thermal stability was enhanced. Therefore, proving their capability as a promising bone bioengineering substitute.

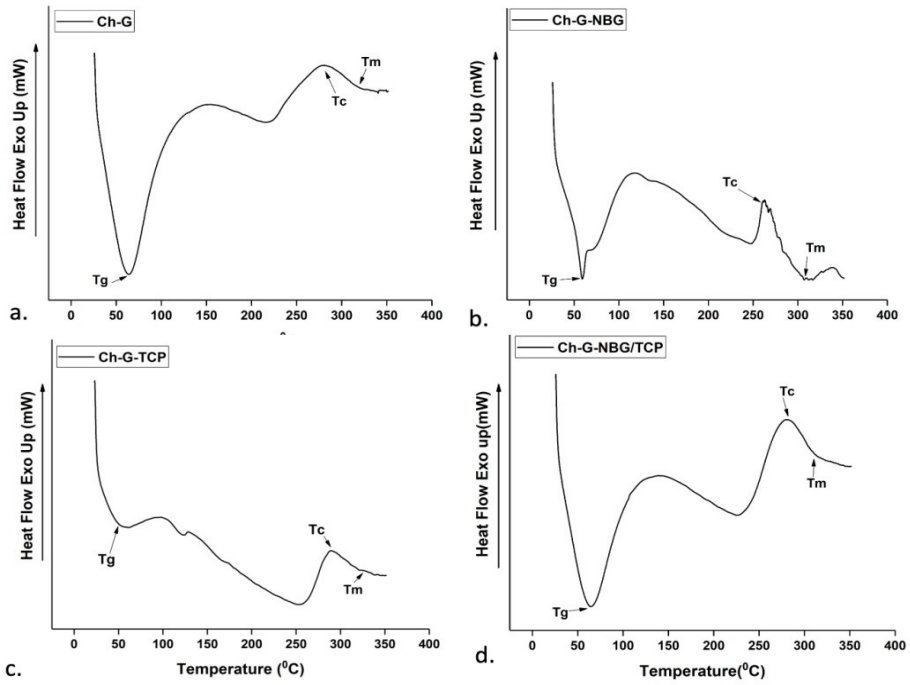

Figure 4.3.6(a-d) DSC graph for the developed scaffolds showing their thermal stability at a higher and lower temperature.

Cytocompatibility of prepared scaffolds

Cell adhesion, migration and proliferation are the three main components of cell growth. Fig.4.3.7 represents the cell growth of the MG-63 cell line in a complete growth medium over the four different samples (Ch-G-NBG, Ch-G-TCP and Ch-G-NBG/TCP) including the control scaffold (Ch-G). It shows the cell growth over the sample on the 3rd, 5th and 7th day. From this figure, it is evident how cell growth has improved after the addition of NBG and ß- TCP over the scaffolds. Crosslinking of the scaffolds has greatly impacted the overall mechanical strength of the samples which has indirectly affected the composite's cell proliferation tendency (Marin et al., 2020). Higher toughness is also proven to induce osteogenesis and therefore the cell growth over the scaffolds has enhanced which proves to be effective for bone tissue regeneration (Shuai et al., 2018; Tarafder et al., 2015). Recently one of the studies where 3D-printed TCP scaffolds were prepared and incorporated with SrO and MgO showed enhanced mechanical strength which also led to better cell adhesion and osteogenic differentiation (Tarafder et al., 2015). Therefore, scaffold with 1:1 ratio of NBG and ß-TCP can be a perfect biomaterial for bone tissue engineering applications.

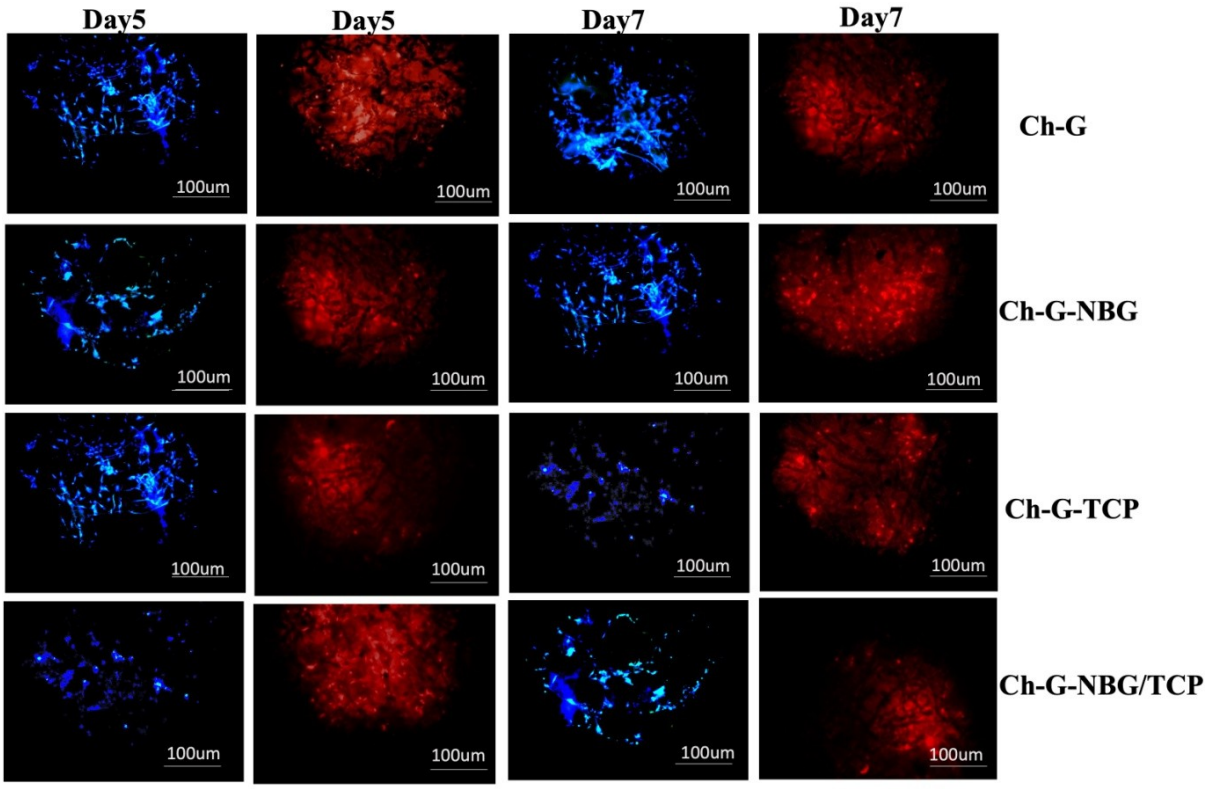

Figure 4.3.7: DAPI and AOPI images of Ch-G, Ch-G-NBG, Ch-G-TCP and Ch-G-NBG/TCP scaffolds on the 5th day and 7th day

Cell viability of MG-63 cells

Fig.4.3.8a illustrates the cell metabolic activity of the MG-63 cell line. MTT assay showed the enhanced cellular viability of the MG-63 cell line in all four samples including the control (Ch-G) for 7 days culture. There was a continuous increase in the cellular growth of MG-63 cells with the addition of NBG, ß-TCP and NBG/TCP composite. It is observed in Fig.4.5a that the addition of the crystalline ceramic components into the scaffold samples resulted in relatively higher cellular metabolic activity with increasing days. However, in the control sample, the cell metabolic activity was around 75 ± 12.1% on the 7th day of culture, while for NBG/TCP composite it appeared to be 95 ± 9.8% on a similar day. Similarly, for NBG incorporated scaffold (Ch-G-NBG) cell metabolic activity was found to be 90 ± 9.1% and for ß-TCP based scaffold (Ch-G-TCP) it came out to be 85 ± 9.4%. Although, the cell metabolic activity percentage was slightly lower for ß-TCP incorporated scaffold in comparison to Ch-G-NBG scaffold yet the steep rise in it proved that the cell viability of osteoblast cells was gradually enhanced after the addition of ß-TCP and NBG. Since nanobioglass exhibits osteogenic properties therefore it can be assumed that cell metabolic acitvity was enhanced due to this property (Durgalakshmi et al., 2014). Similarly, ß-TCP also possesses the inorganic components of bone which are calcium and phosphate which forms 60% of bone architecture

(Cichoń et al., 2019). Hence, all the developed scaffolds were found suitable for osteoblast cell culture. The present study also suggests that ß-TCP and NBG together play an essential role in enhancing cellular viability due to their crystalline nature. Therefore, NBG and ß-TCP together might prove to be promising scaffolds for bone tissue regeneration applications.

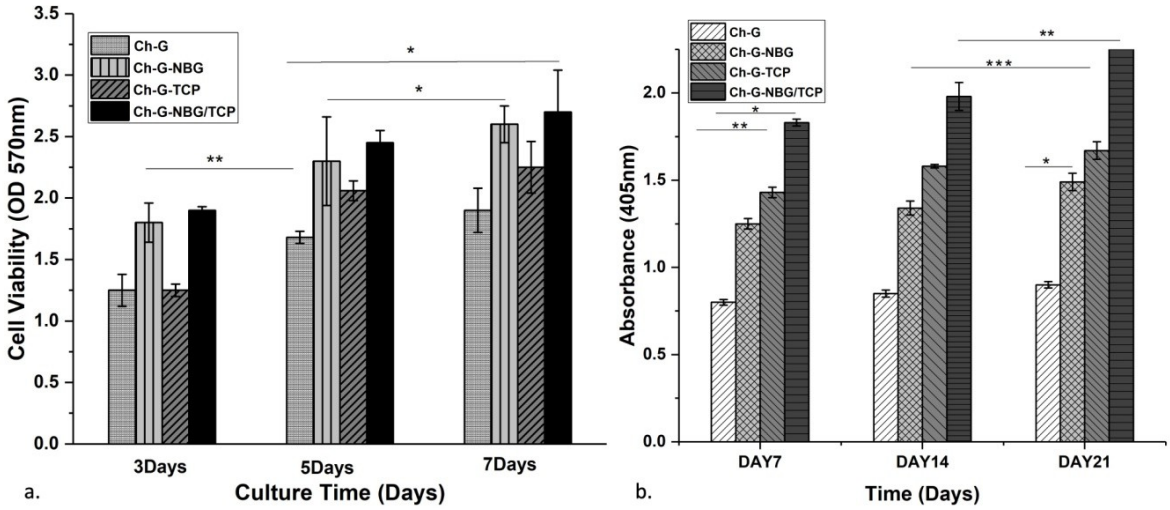

Figure 4.3.8(a)- MTT assay of developed scaffolds, Fig.4.3.8(b)- ALP activity of MG-63 cells over developed scaffolds.

Alkaline Phosphatase Assay

Alkaline phosphate assay was performed to assess the alkaline phosphate activity of osteoblast cells cultured over NBG and ß-TCP based scaffolds. Fig.4.3.8b illustrates the ALP activity of osteoblast cells. It shows that after culturing of cells for 7 days, the osteogenic marker was significantly enhanced in the case of Ch-G-NBG/TCP scaffold. But no such difference was observed in the case of Ch-G scaffolds. However, ALP activity over Ch-G- NBG/TCP scaffold was seen to be essentially higher when compared to Ch-G-NBG and Ch- G-TCP scaffolds on day 14.

Furthermore, NBG and ß-TCP played an essential role in ALP activity enhancement and this was observed due to the release of osteogenic mineral (bioactive silicon) from NBG and calcium phosphate from ß-TCP (Sulaiman et al., 2013; Westhauser et al., 2020). ß-TCP is usually known for its resorbable nature and favourable solubility and it has been shown to replace the host bone tissue also. It was observed from previous literature that it stimulates osteogenic differentiation by upregulating the stimulation of bone biomarkers like collagen type I and ALP. This can be observed in Fig.4.3.8b also where after the incorporation of ß-TCP into the scaffolds, the osteogenic differentiation has tremendously improved. It was due

to the ionic discharge of the components which led to an increased pH value which ultimately facilitated the precipitation of Ca^{2+} and PO_4^{3-} ions. It led to an alkaline environment which is proven to be beneficial for osteoblast cell differentiation and growth. The increased pH also suppressed the growth of osteoclasts and thereby led to enhanced ALP activity (Zheng et al., 2021).

Alizarin Red S assay

Biomineralization activity of the MG-63 cells was estimated using Alizarin Red Stain assay. Fig.4.3.9a shows the cell culture over scaffolds for the 7th and 14th days and it is clear by the red colour fluorescence that on day 14 the biomineralization activity of the osteoblast cells was higher. Especially in the case of Ch-G-NBG, Ch-G-TCP and CH-G-NBG/TCP scaffold, the mineralization appeared to be in a similar range which suggests that after ß-TCP and NBG addition in the scaffolds, the osteoblast's mineralization enhanced. Fig.4.3.9b illustrates the graphical representation of the ARS staining of osteoblast cells cultured over developed scaffolds. It was observed that after the incorporation of nanobioglass and ß-tricalcium phosphate in the Ch-G scaffold, the biomineralization was accelerated through Ca^{2+} and PO^{4-} release when dissolved under culture conditions (X. Wu et al., 2020). This can be observed in the microscopic images. After day 14, the mineral deposition was quite higher in all the cases due to the bioceramics phases present inside the scaffold compositions except the Ch-G scaffold and therefore a high red colour intensity was observed in all the scaffolds. Hence, an in-vitro biomineralization study performed using Simulated Body Fluid confirms ECM influence the process of extracellular apatite deposition which is a cell-independent process. Thus, the *in-vitro* mineralization study shows cell-arbitrated apatite accumulation over the fabricated scaffold (Singh et al., 2019).

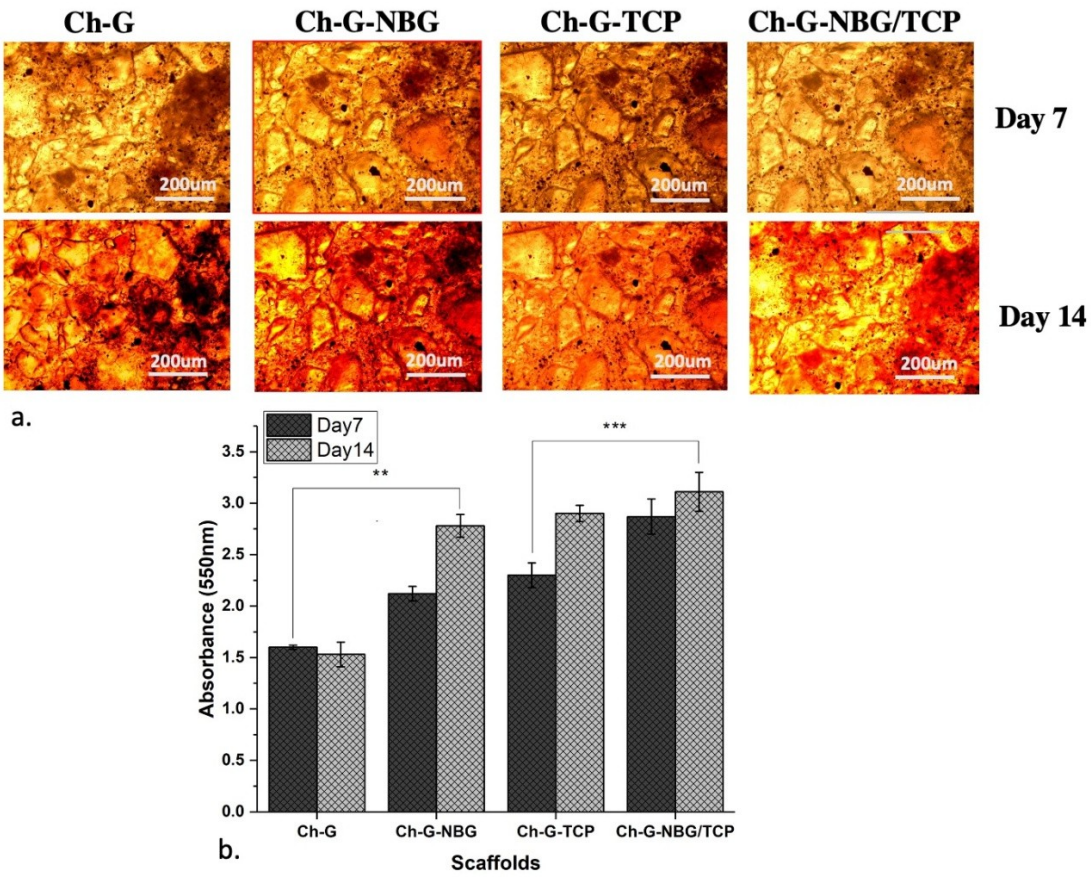

Figure 4.3.9(a)- Inverted phase contrast microscopic images of Alizarin Red S. stained cultured cells for 2 weeks.Fig.4.3.9(b) Biomineralization of scaffolds cultured for 2 weeks

Cell attachment (SEM)

These are the SEM micrographs of the cell-seeded scaffolds. Fig.4.3.10 illustrates the cell spreading over Ch-G, Ch-G-NBG, Ch-G-TCP and Ch-G-NBG/TCP scaffolds. They show how the osteoblast cell is attached to the scaffolds surface. This attachment might be due to the roughness provided by the TCP and NBG incorporated into the biocomposite. Since the rough surface promotes osteogenesis therefore it can be clearly observed in this image how the cell spreading is occurring on all the developed scaffolds. The combination of hydrophilic chitosan and gelatin also promotes cell adhesion which is evident in this image. SEM image of the cell-seeded scaffolds shows that these scaffolds are suitable for osteoblast cell adhesion and proliferation.

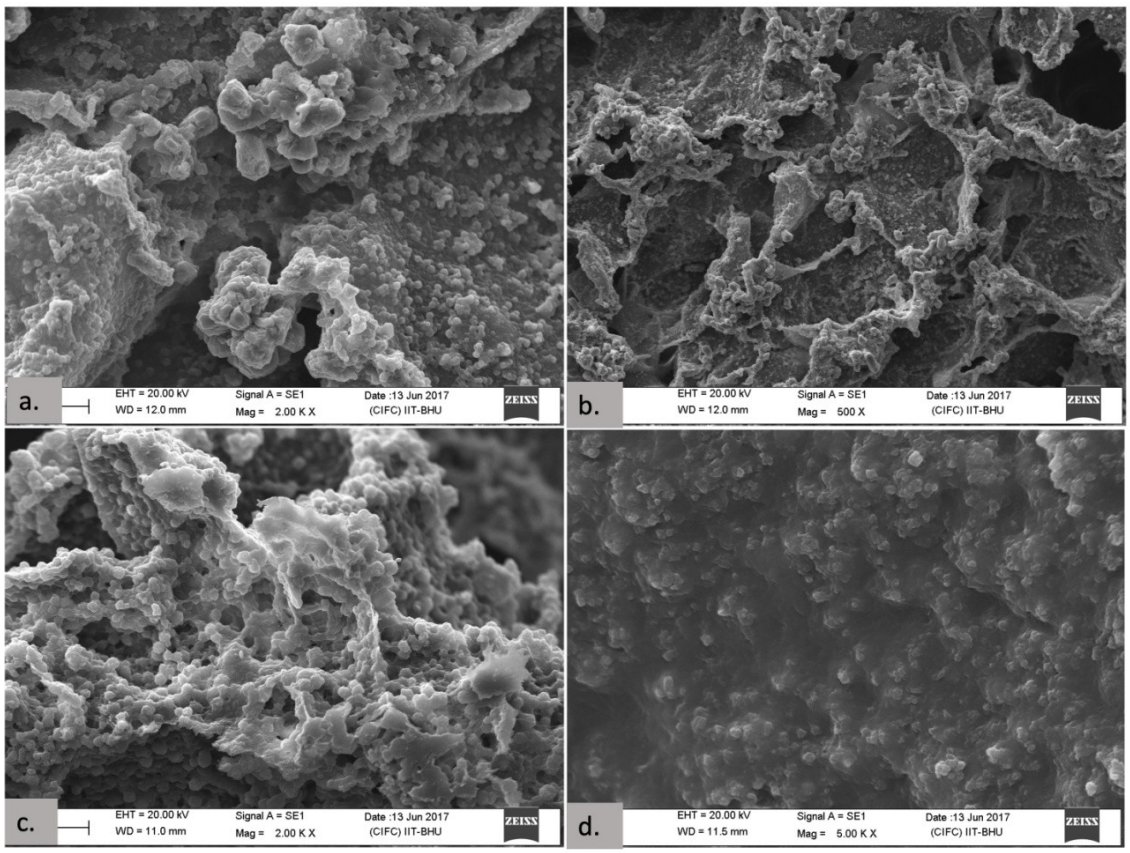

Figure 4.3.10(a)-SEM image of cell attachment and spreading over Ch-G scaffold. Fig4.3.10(b)- SEM micrograph of cell spreading over Ch-G-NBG scaffold. Fig.4.3.10(c)- Cell spreading over Ch-G-TCP scaffold. Fig.4.3.10(d)- Cell spreading over Ch-G-NBG/TCP scaffold.

Chapter 4.4

Development and Evaluation of Graphene oxide and Nanobioglass based scaffold for Bone Tissue Regeneration

4.1. Results and Discussion

Graphene oxide offers a distinct opportunity in the field of biomedical engineering owing to its exceptionally high mechanical strength, excellent electrical conductivity, high optical transparency, and favourable biocompatibility. In this article, nanocomposite biocompatible chitosan gelatin based graphene oxide and nanobioglass infused scaffolds (chitosan/gelatin/nanobioglass/graphene oxide) Ch-G-NBG-GO were successfully fabricated through freeze drying technique (-40ºC) and evaluated for various physicochemical and biological properties. Previously we have obtained scaffold with good porosity and bioactivity due to NBG incorporation but we wanted improve the mechanical strength further and therefore, we conducted this experiment wherein we have used GO and NBG , two new additives for our study. The prepared Ch-G-NBG-GO composites have been investigated for their structural, physiochemical, and surface morphology via X- ray Diffraction (XRD), Scanning Electron Microscope (SEM), Fourier Transform Infrared spectroscopy (FT-IR), thermogravimetric analysis (TGA), Energy- dispersive X-ray Spectroscopy (EDX) and, Differential Scanning Colorimetry (DSC) respectively. The morphological analysis showed the porous interconnected network of scaffold formed. Average pore size for the Ch-G-NBG-GO scaffolds were in between 90 to 120 μm, which was very close to the control scaffolds. XRD data revealed the successful incorporation of NBG and GO and distribution across the scaffolds. Porosity of the fabricated scaffolds were in the range between 75.3% to 77.3% which was very close to the control scaffold with 79% porosity. The studies also reveal that after GO incorporation, the weight loss reduced (0.11 ± 0.02 to 0.095 ± 0.03), scaffolds were firmly stable at room temperature even after a long duration of 28 days. The crystallinity added to the scaffolds due to addition of GO nanoparticles improved the mechanical strength of these scaffolds. The compressive modulus changed from (5.7 to 8.51) MPa after GO addition. Swelling ratio changed drastically especially in case of Ch-NBG-90%GO (4.9 ± 0.04 to 4 ± 0.01). DSC and TGA data revealed the thermal stability of GO-incorporated scaffolds due to the proper interaction between GO/NBG with Chitosan-gelatin blend. The scaffold's potential for bone tissue engineering was evaluated by testing its cytocompatibility for MG-63 cell line. It revealed suitable cell attachment and proliferation of cells compared to the Ch-G-NBG scaffold. MTT assay showed that Ch-G-NBG-GO scaffold below 90%GO concentration possess best biocompatibility. But in case of Ch-G-NBG-90%GO scaffold, the cell proliferation was reduced when compared to control scaffolds.

Characterization of Graphene oxide

Fig.4.4.1 shows the characterization of graphene oxide nanoparticles used in the development of the chitosan-based scaffolds. Graphene oxide was procured from Sigma and it was a black color fine powder as seen in Fig.4.4.1a. X-ray diffraction, Fourier Transform Infrared Spectroscopy and Transmission Electron Microscopy were done to characterize the structure and properties of graphene oxide obtained from Sigma. XRD peaks at $2\theta=12$ show the crystallinity of graphene oxide procured from Sigma (Fig.4.4.1b). It shows a clear 0 0 1 crystal plane at a spacing of 8.33Å which is graphene oxide. TEM image in Fig.4.4.1c shows the thin sheets of graphene oxide formed in the range of 100nm. The transparent layers indicate thin layers of graphene oxide present when the electron beam is transmitted. In Fig.4.4.1d diffraction pattern of the same graphene oxide is demonstrated showing two overlapping layers of graphene oxide. One layer at 1 0 0 and one at 1 1 0 crystal plane. Fig.4.4.1e represents the thermogravimetric graph of graphene oxide. It shows the degradation temperature is around 350°C with a total weight loss of 1.8mg. Lastly, the FTIR of graphene oxide is shown in Fig.4.4.1f. The FTIR bands at 3434.59cm^{-1} due to OH stretching, 2921.74cm^{-1} and 2849.81cm^{-1} due to C-H stretching correspond to graphene oxide. Bands at 1726.10cm^{-1} due to C=O bonding and 1627.64cm^{-1} due to C=C bonding were also observed. Then the peaks at 1387.41cm^{-1} and 1084.17cm^{-1} observed due to C-O bonding clarify that the procured graphene oxide was suitable for further study.

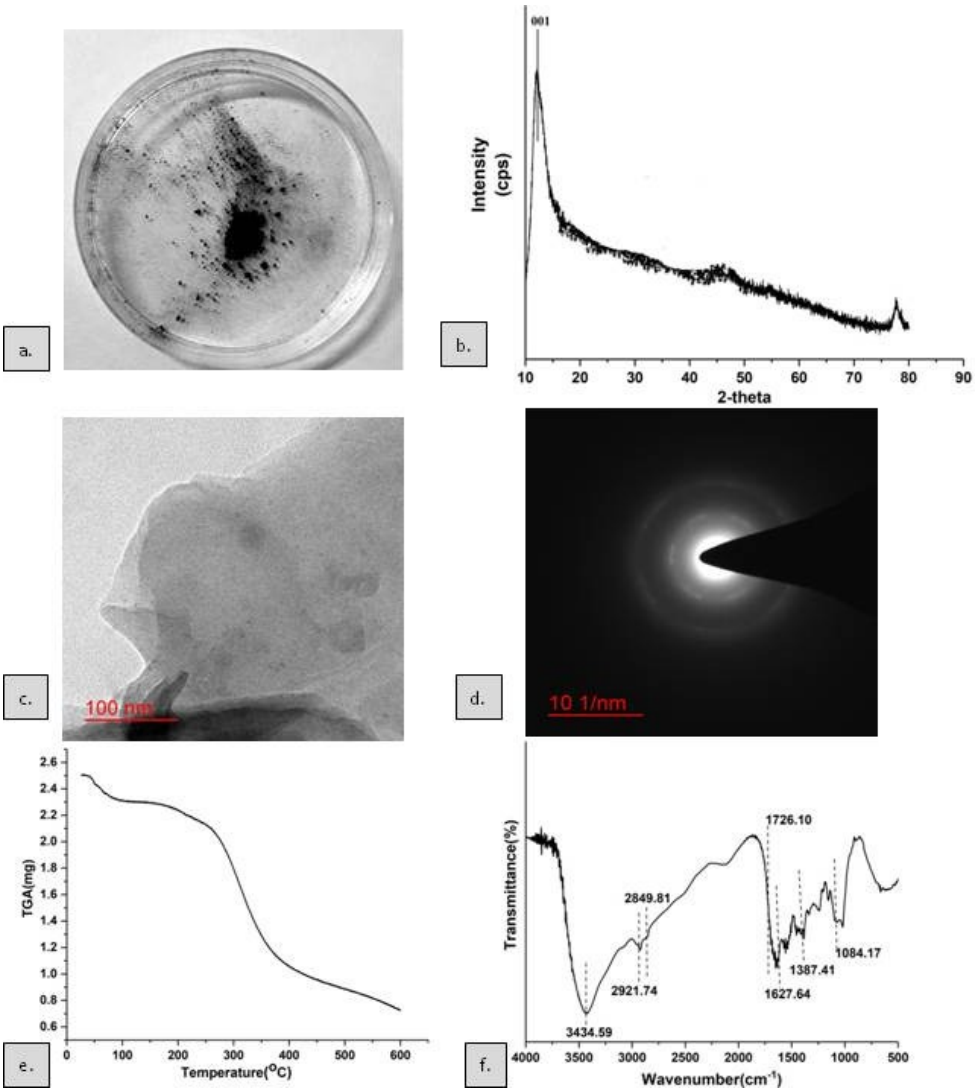

Figure 4.4.1(a)-Photographic image of graphene oxide utilized for scaffold fabrication. Fig.4.4.1(b)-XRD spectra of graphene oxide. Fig.4.4.1(c)-TEM micrograph of graphene oxide. Fig.4.4.1(d)-SAED pattern of graphene oxide for scaffold development. Fig.4.4.1(e)-TGA graph of graphene oxide. Fig.4.4.1(f)-FTIR graph of graphene oxide used in the experiment

Morphological analysis of developed scaffolds

Fig.4.4.2a depicts the physical structure of manufactured scaffolds, and Fig.4.4.2b shows SEM micrographs of the developed scaffolds at 100µm and 200µm scale. A slight greyish colour was seen after the addition of graphene oxide nanoparticles in these scaffolds. The porous structure of scaffolds is prominent in all the samples. Pore size between 90µm to 120µm, was the average pore size observed in the graphene-based scaffolds. The micro-network formation took place after the addition of GO, and this might be because of the intercalation of GO with gelatin and nano-bioglass. A more firm and harder scaffold structure was observed as seen in

Fig.4.4.2a. The pore size was also reduced after the addition of nanobioglass, as seen in Fig.4.4.2b, whereas in the Chitosan-Gelatin scaffold, the pore size was between (175-190) μm.

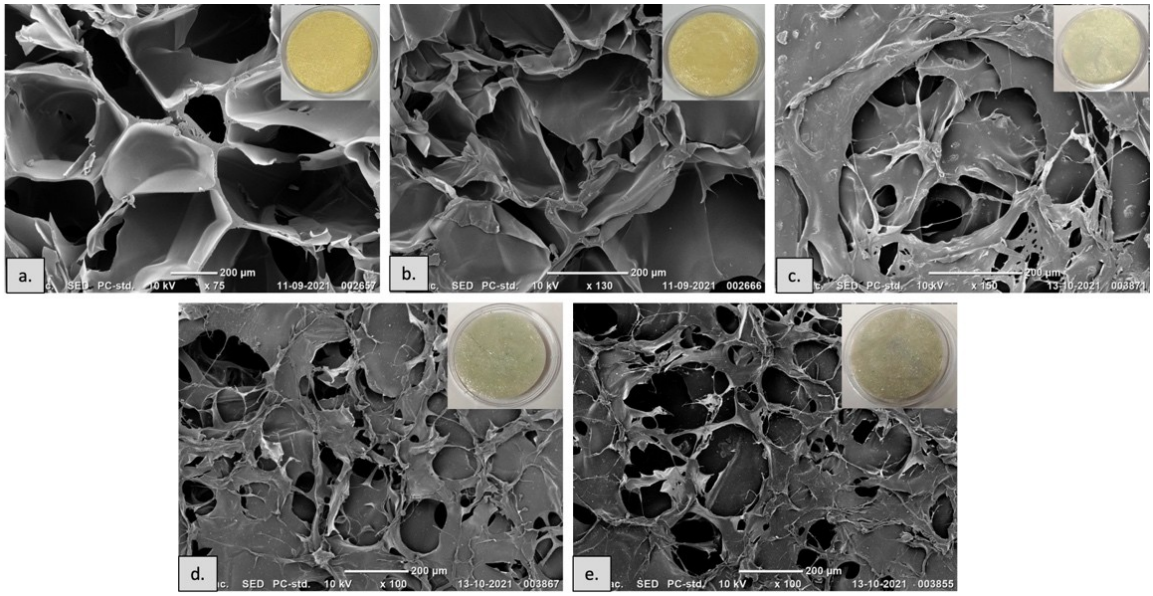

Figure 4.4.2: Digital images and SEM micrographs of developed scaffolds. Fig.4.4.2(a)-SEM image of Ch-G scaffold. Fig.4.4.2(b)-SEM image of Ch-G-NBG scaffold. Fig.4.4.2(c-e)-SEM image of Ch-G- NBG 30% GO, 60% GO and 90% GO respectively

Structural and functional analysis of developed scaffolds (FTIR and XRD)

Fig.4.4.3a illustrates the Fourier Transform Infrared spectra of developed scaffolds. It shows a prominent band at around 3429cm^{-1} wavelength, which is attributed to the OH bond stretching (Bozorgi et al., 2022; Khalili, 2016). The C=O stretching at around 1704 cm^{-1} corresponds to intramolecular H-bonds of the GO. This peak got enhanced due to the bonding between oxygenated chitosan and carboxy groups of the scaffolds (Valencia et al., 2018). Distinct band formed at 1550 cm^{-1} band was observed due to C=N bond formation occurring due to interaction between C-G. The peak shift from 1500 to 1800 cm^{-1} indicated the electrostatic interactions between the amide groups of C-G and carboxylic groups of GO (Saravanan et al., 2017). The firm, broad band between 2800-3000 cm^{-1} wavelength represents NH stretching, which might be present due to the exchange of nano-bioglass with chitosan and gelatin. The peaks observed at around 802-1058 cm^{-1} correspond to nanobioglass. Overall, the FTIR spectra reveal the presence of GO, NBG and Ch-G interaction and their specific functional groups in the Ch-G-NBG-GO composite scaffolds.

Fig.4.4.3b shows the XRD spectra for fabricated scaffolds. Characteristic peaks of graphene oxide in graphene oxide impregnated scaffolds diminished slowly with gradually intensified

interaction with the composite biomaterial. Hence it may provide better strength to the overall design of the scaffold. Peaks for nano bioglass that were supposed to be observed at 2θ = 30-35 and 40-50 also vanished representing its blend formation in the chitosan-gelatin solution. The broad band between 2θ =20-30 describes the amorphous nature attained due to chitosan and gelatin interaction that shares the same peak.

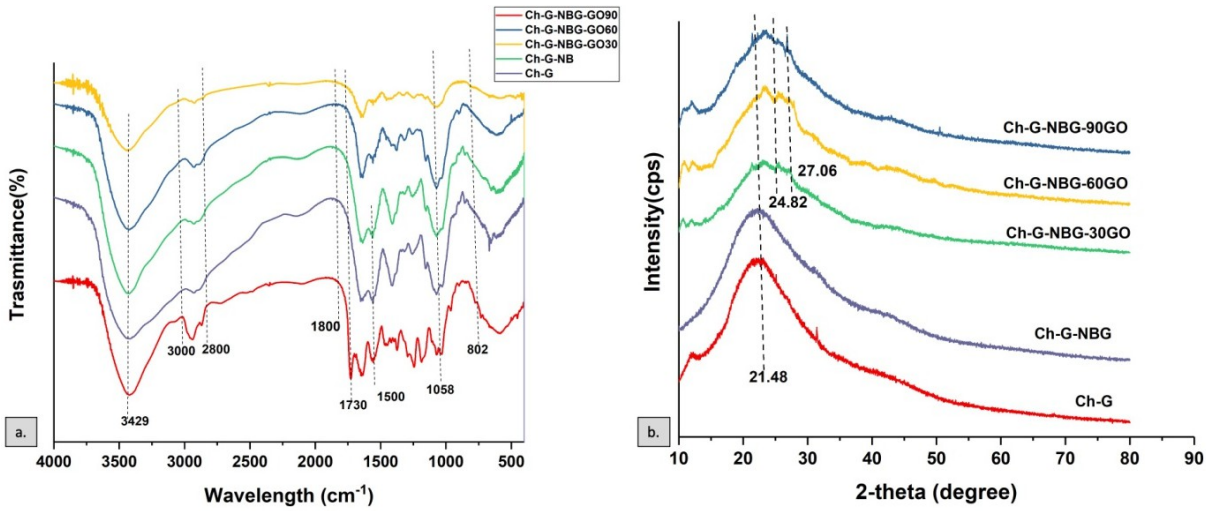

Figure 4.4.3(a-b)-FTIR and XRD graph of developed scaffolds without GO and with GO

Thermal stability analysis of synthesized nanocomposite scaffolds (DSC)

Similarly, DSC was performed to test the scaffolds' thermal stability (Fig.4.4.4). The control scaffold Ch-G-NBG glass transition temperature was 75°C, as illustrated in Fig.4.4.4. The glass transition temperature rose when graphene oxide nanoparticles were mixed into the porous scaffolds. The use of GO in blended scaffolds may raise the nanocomposite scaffolds' glass transition temperature by increasing the composite solution's stable blend. In addition, with the inclusion of GO, the melting temperature of the nanocomposite scaffolds also enhanced. For the Ch-G-NBG scaffold, there was an exothermic step trend at 265°C with an enthalpy of 12.38 J g^{-1}. There was an exothermic upside step trend at 300°C for 30% Ch-G- NBG-GO, with an enthalpy of 59.81 J g^{-1}. It was the case for all the GO-based scaffolds, i.e., 60% and 90%. Their exothermic step trend was visible at around 300°C with increased enthalpy compared to the control scaffold. It was observed that for C-G scaffold the melting started very early around 220°C and for GO based scaffold the melting started at around similar temperature of 330°C. It shows that the graphene oxide-based scaffolds were more crystalline than Ch-G-NBG scaffolds, with higher enthalpy indicating a higher degree of crystallization.

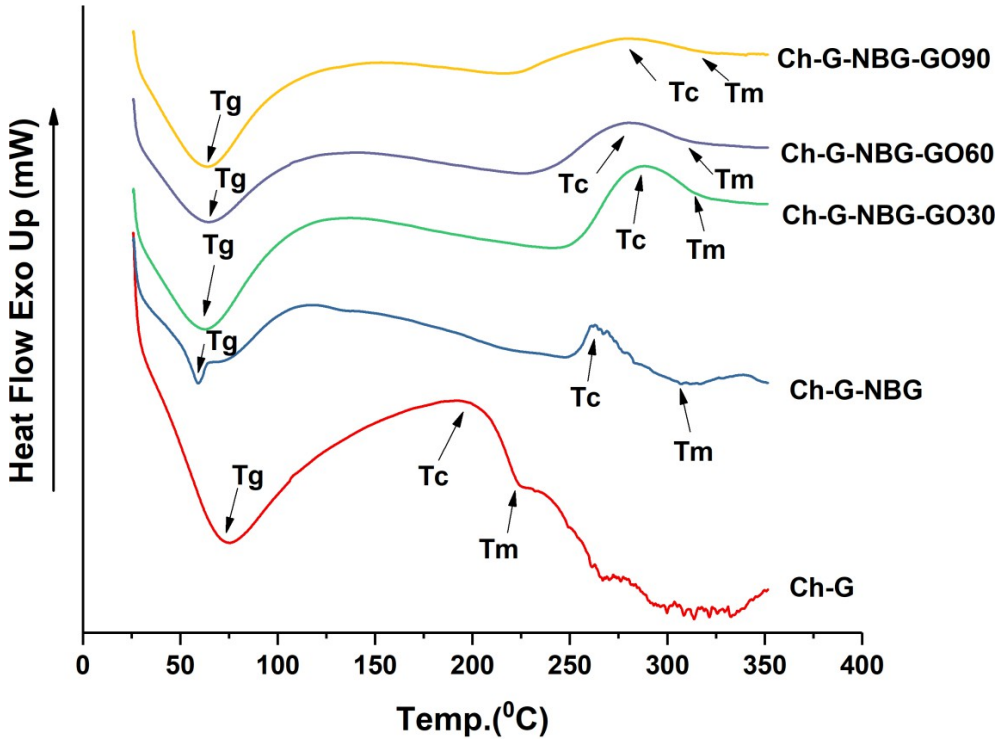

Figure 4.4.4: Thermal stability analysis of developed scaffolds.
DSC graphical evaluation of developed scaffolds with and without GO nanoparticles

Water retention evaluation of developed scaffolds

The water retention capacity of the prepared samples was tested by immersing the scaffolds in PBS solution at physiological conditions. Then, the weight gain of the sample was estimated using a weighing scale. Thus, determining its stability in *in-vitro* conditions (Fig.4.4.5b). This study is essential in examining cell infiltration during cell culture in the artificial 3D microenvironment (Farshi et al., 2014). The higher the swelling capacity, the better will be the cellular infiltration. It was noticed that after crosslinking the scaffolds with EDC-NHS, the scaffolds attained improved stability (Shepherd et al., 2015). The water retention capacity of the Ch-G-NBG scaffold and Ch-G-NBG-GO scaffolds with varying GO concentrations showed a similar pattern (Fig.4.4.5b). They increased continuously with running time intervals. However, the water uptake capacity of Ch-G-NBG-90%GO was reduced from 4.9 ± 0.04 to 4 ± 0.01 compared to the positive control and other scaffolds. Higher the stability, the higher the biodegradation rate and, therefore, the infiltration rate of the cells. Hence, it shows that incorporating graphene oxide nanoparticles enhanced the stability of fabricated scaffolds.

Biodegradation study of GO nanoparticles-based scaffold

A biomaterial's degradation and stability are yet another criterion of a promising artificial extracellular matrix for tissue regeneration. Therefore, a degradation study of the prepared scaffolds was performed at physiological conditions to understand their biocompatibility. Fig.4.4.5a. demonstrates the biodegradation of the fabricated scaffolds. The samples were cut into 2x2 cm^2 sections and then dipped into lysozyme solution made in PBS for 28 days. The scaffolds turned out to be stable even after the incorporation of GO nanoparticles. It was observed that the Ch-G scaffold showed an increased biodegradation rate with increasing time intervals. They started degrading enormously after 21 days. The degradation rate decreased after the addition of nanobioglass. But a pattern was observed which showed an increasing degradation rate with increasing time duration. However, a significant change was observed in the degradation rate after incorporating the graphene oxide nanoparticles, as seen in Fig.4.4.5a. In the case of Ch-G-NBG-30%GO, the degradation rate was comparatively lesser to Ch-G-NBG scaffold on the 28th day. Ch-G-NBG-60%GO degradation was comparatively slower when compared to Ch-G-NBG-30%GO. While in the case of 90%GO, the degradation rate was a little lower than other GO based scaffolds. They were quite stable to be held by forceps.

Furthermore, it shows that all the scaffolds were stable except Ch-G scaffolds. But after adding graphene oxide nanoparticles, a noticeable change was observed in the scaffolds. It might be due to the crystalline nature imparted due to GO nanoparticles addition. The rate of degradation lowered within the range of cancellous bone structure. But in particular, the rate of degradation was reduced, and the weight loss was reduced to 0.95 ± 0.03 on the 28th day of degradation in the case of 90% graphene oxide-based scaffold.

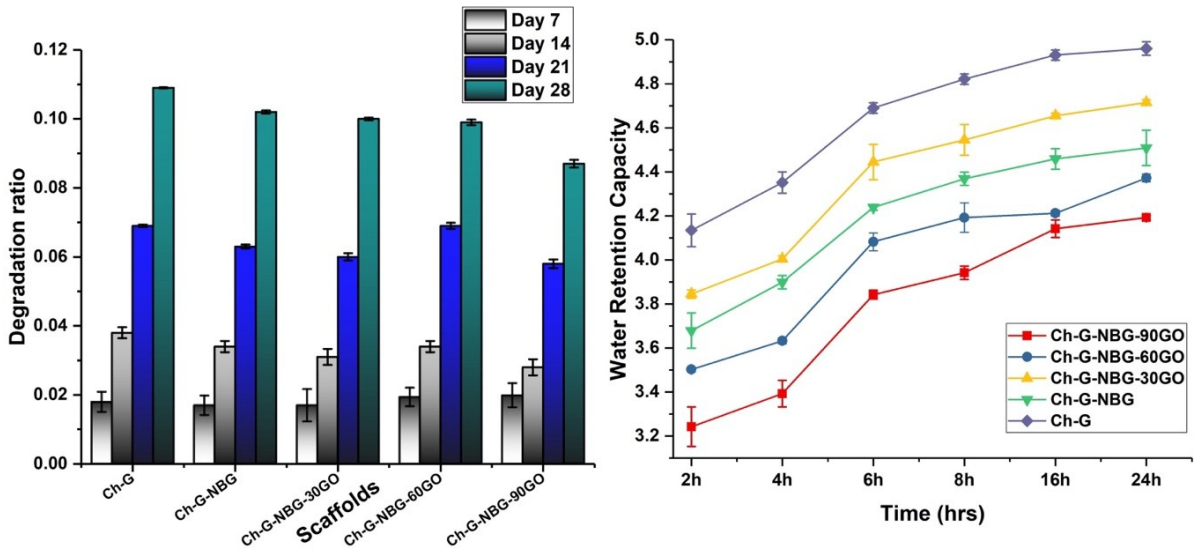

Figure 4.4.5(a): Biodegradation study of fabricated scaffolds for 28 days. Fig.4.4.5(b). Water retention capacity analysis of manufactured scaffold including GO based scaffolds.

Porosity evaluation of fabricated scaffolds

It was seen that Ch-G-NBG served as a positive control for the Ch-G-NBG-GO scaffolds with different percentages of GO (Fig.4.4.6a). It was observed that Ch-G scaffold possessed the average value for porosity which is around 90%. From the data, it was evident that the porosity reduced after the addition of NBG into the Ch-G blend to 79%. But the porosity of Ch-G-NBG30%GO, Ch-G-NBG-60%GO and Ch-G-NBG-90%GO came out approximately in a similar range, 77.3%, 75.12% and 75.3%, respectively. The porosity exhibited by all the developed scaffolds were in range for bone tissues. But after the addition of graphene oxide nanoparticles and nanobioglass, the porosity observed minor modifications. But from previous studies it was seen that the porosity range was effective for bone tissue regeneration applications (S. Wu et al., 2014). It tells that there was no such effect on the porosity of the scaffolds after the addition of graphene oxide nanoparticles.

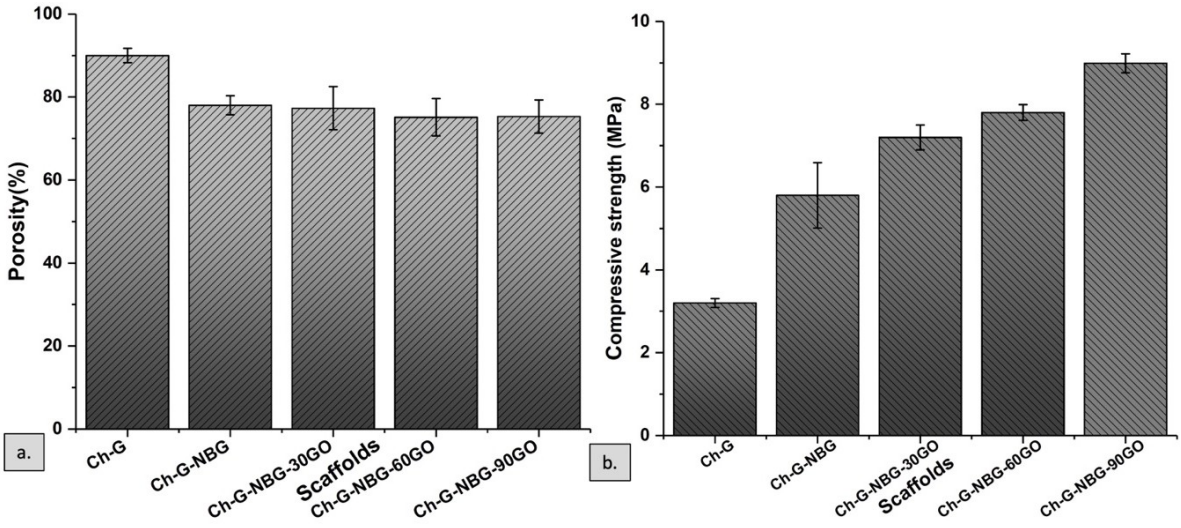

Figure 4.4.6(a): Porosity evaluation graph of developed scaffolds. Fig.4.4.6(b). Compressive strength graph for prepared scaffolds with GO and without GO nanoparticles

Mechanical strength of developed scaffolds

After the porosity estimation of fabricated scaffolds, it was evident that porosity was not affected by the inclusion of graphene oxide nanoparticles. But then it became essential to understand the effect on the compressive strength of the scaffolds. Therefore, a mechanical strength evaluation of all the scaffolds, including the control, was performed (Fig.4.4.6b). Compressive modulus was plotted for all the scaffolds. The compressive strength of the Ch-G scaffold was 3.7MPa which was significantly less. But after the addition of nanobioglass, the

strength improved to a certain extent and became 5.7MPa. Later a sudden increase in the compressive strength was observed in Ch-G-NBG scaffolds with 30%, 60% and 90% GO. It came out to be 7.2MPa, 7.6MPa and 8.51 MPa, respectively. Because of the incorporation of GO into the developed scaffolds, all three scaffolds with different concentrations of GO exhibited satisfactory compressive strength, which was in range for the cancellous bones. On the other hand, the scaffold with the highest percentage of GO, i.e., 90%, possessed the highest mechanical strength. This shows that it was the most suitable scaffold for bone tissue regeneration.

Fig.4.4.7 shows the stress-strain plot for the prepared scaffolds. Fig.4.4.7a represents a Chitosan gelatin scaffold with approximately 35% strength. Then after NBG addition, the scaffold immediately gained better strength of around 40%. But it was interesting to know that after the incorporation of graphene oxide nanoparticles into the scaffolds, the mechanical strength showed a significant improvement of around 80%. This was almost the same in all the cases including 30%,60% and 90% GO scaffolds. It depicted that the goal of improved mechanical strength was achieved after the addition of graphene oxide into the composite solution.

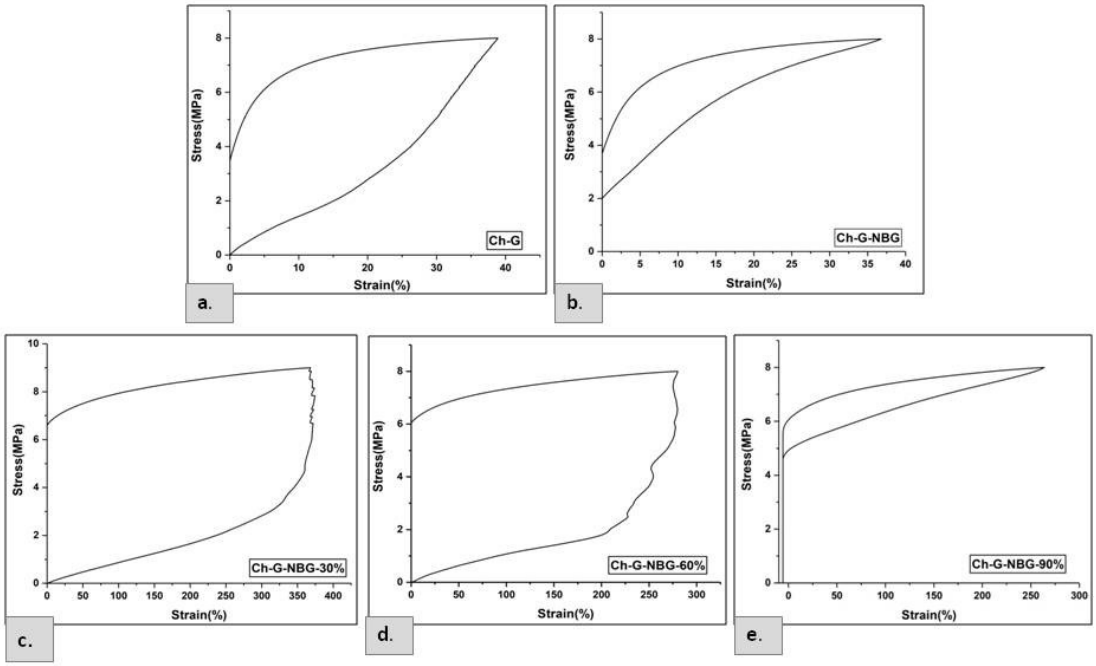

Figure 4.4.7: Stress-strain plot for fabricated scaffolds.Fig.4.4.7(a)- Stress-strain plot for Ch-G scaffold. Fig.4.4.7(b)- Stress-strain curve for Ch-G-NBG scaffold. Fig.4.4.7(c-e)-Stress-Strain curve for Ch-G-NBG-30%GO, 60%GO and 90%GO respectively.

Cytocompatibility of MG-63 cells over developed GO incorporated scaffolds

Cell behavioural study is one of the significant parameters that are considered while designing a cell-scaffold construct for any tissue. Therefore, a microscopic analysis of the cultured MG-63 cell line was done to determine the suitability of fabricated nano-biocomposite scaffolds. Cell attachment and spreading of MG-63 cells were studied on the developed scaffolds for 7 days (Fig.4.4.8). Fluorescent microscopy revealed that the cells were proliferating and growing excellently and turned confluent till the seventh day of culture. The confluency level was different for distinctive scaffolds. The cells were found remarkably attached over Ch-G and Ch-G-NBG scaffolds. At the same time, they reached 70% confluency in the case of Ch-G-NBG-30GO and Ch-G-NBG-60GO till the end of the seventh day. It can be depicted from the cell behaviour that the degradation products of the biocomposite scaffolds affect the cellular growth of MG-63 cells also. In the case of Ch-G- NBG-90GO, the cell proliferation rate was average compared to the positive control. But overall, the cell attachment and proliferation were evident by the live-dead assay (Fig.4.4.8). These images showed that all the samples promoted cell attachment and spreading, and the morphology was intact over these scaffolds. Thus, these results demonstrate that the fabricated cell-scaffold construct with different concentrations of graphene oxide is cytocompatible and favourable for cell attachment and proliferation. As seen by previous studies GO nanoparticles promote accelerated growth of osteoblast cells (Qi et al., 2014; C. Wu et al., 2015). Thereby we can predict that our GO based scaffolds promotes the constant cellular growth within the 3D micro-network.

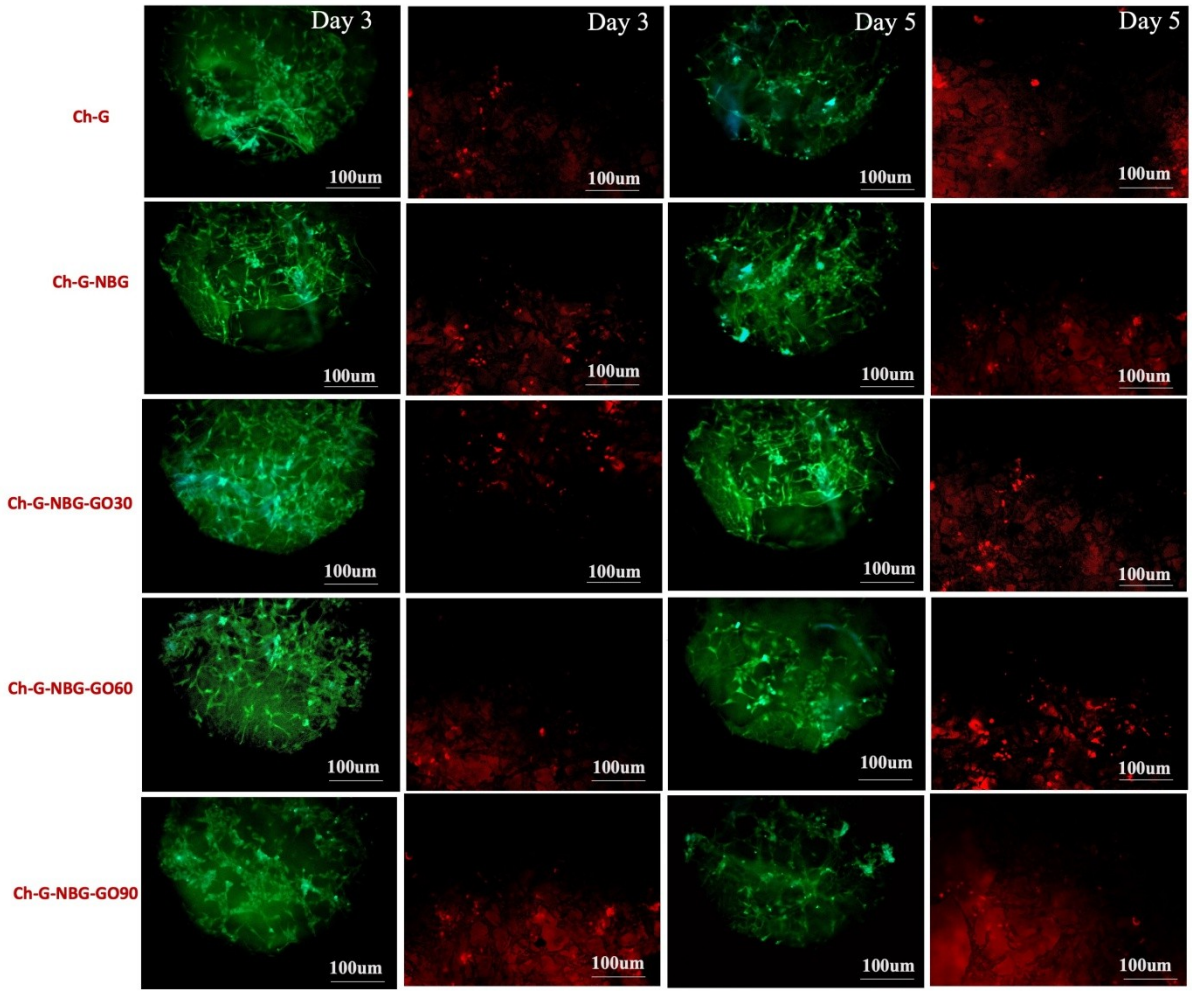

Figure 4.4.8: Live and dead assay of 3rd and 5th day of cell-scaffold culture over developed scaffolds.

MTT assay for studying cell metabolic activity over developed scaffolds

MTT assay showed that cell viability was very good for all the cell-laden scaffold constructs (Fig.4.4.9a). Cellular viability was good in the Ch-G-NBG scaffold, which served as a positive control for all the other GO-incorporated scaffolds. Ch-G-NBG scaffold possessed the highest cell metabolic rate on the fifth day. However, it was seen that even in the case of Ch- G-NBG-30% GO and Ch-G-NBG-60%GO scaffolds, the cellular metabolic rate enhanced on the fifth day compared to the positive control. This might be due to the osteoconductive environment provided by GO and NBG addition to the MG-63 cells. However, the metabolic rate was lower in the case of Ch-G-NBG-90%GO in comparison to the Ch-G-NBG scaffold. However, no significant modification was observed in its metabolic activity when compared to the previous studies. Therefore, this study suggests that cell growth was enhanced after the sudden incorporation of nanoparticles into the scaffolds. But till 60%GO concentration, scaffolds showed promising results which again might be due to the integrin mediated cell adhesion release due to GO addition in the scaffold. On the other hand, 90%GO concentration showed

decreasing metabolic activity of cells, which suggests that after this concentration, they may be cytotoxic to the cells. The MTT assay shows here that cell metabolic activity of the developed scaffolds with GO and NBG possess great potential for bone tissue engineering applications but nanoparticles like GO can be cytotoxic for the osteoblast cells above a certain range and here above 60% GO addition depicts that hypothesis (Cheng et al.,2021).

ALP activity of MG-63 cells over fabricated scaffolds

Fig.4.4.9(b) shows the Alkaline phosphatase activity of MG-63 cells over the constructed scaffolds. After determining the suitability of the prepared scaffolds for cell metabolic activity, it was necessary to estimate the osteogenic differentiation of these cells. In osteoblast studies, the MTT assay ensures that any increase in ALP activity is not due to increased cell death or reduced proliferation, thus validating that the observed ALP activity is genuinely indicative of osteogenic differentiation. Here the ALP activity of MG-63 cells suggested that the cells' osteogenic differentiation was highest on day 21, and it was the same for all the scaffolds including the positive control. For Ch-G and Ch-G-NBG scaffolds also there was a slight enhancement in the ALP activity from the previous study in which we developed Ch-G-NBG/TCP scaffolds. This change is merely due to enzyme Here Ch-G-NBG scaffold served as control for the developed scaffold. It was seen that after incorporating 30%GO into the scaffolds the ALP activity enhanced slightly and similarly it increased for 60% GO scaffold also. In the case of 90% GO-based scaffold also, the osteogenic differentiation increased but very gradually after the 7th day. It might be because of the degradation products of the developed composite scaffold. Since GO nanoparticles also possess good cytocompatibility and NBG is bioactive in nature as observed from previous literature (Durgalakshmi et al., 2014; La et al., 2013; Li & Kaner et al., 2008). This study indicates that GO nanoparticles promote the cellular differentiation, but from previous studies, it is observed that with increasing concentration of GO nanoparticles the osteogenic differentiation is greatly impacted (Zhang et al., 2016). Hence concentration or ratio of GO incorporated for scaffold development should be in an optimal range and beyond 60% composition.

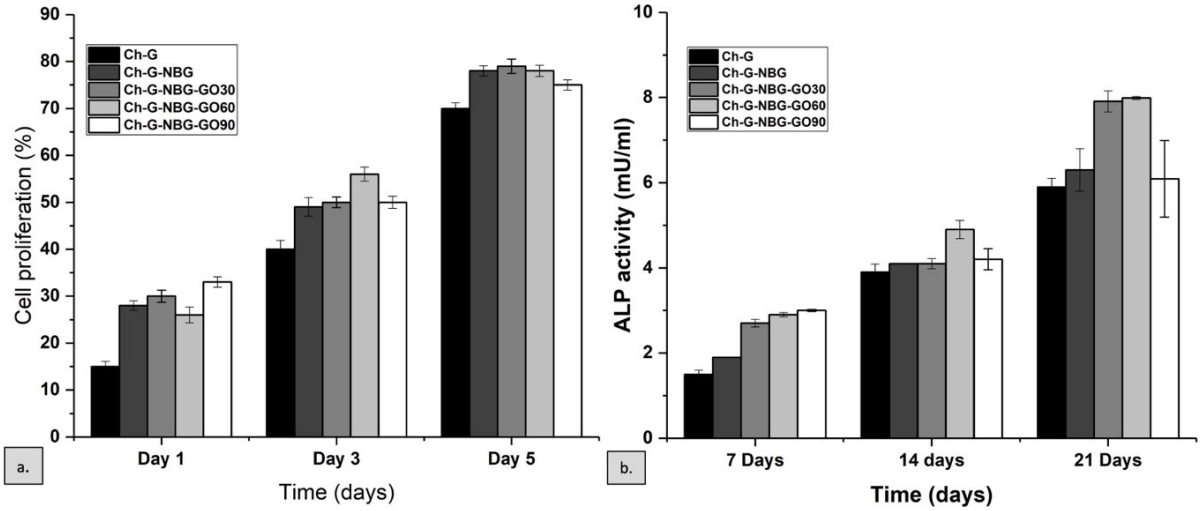

Figure 4.4.9a): MTT assay graphical representation for all the scaffolds. Fig4.4.9(b). Graphical representation of ALP activity of developed scaffolds for 21 days.

SEM of cell-seeded scaffolds

SEM of cell-seeded scaffolds in Fig.4.4.10 shows how cell adhesion and spreading are occurring. These SEM micrographs display the MG-63 cells adhesion and proliferation over the Ch-G-NBG scaffolds and also Ch-G-NBG scaffolds with 30% GO, 60% GO and 90% GO. It shows the cells adhesion over the developed scaffolds on day 7 and it clearly signifies how after the incorporation of GO nanoparticles osteoblast cell line proliferation is occurring. Hence, it can be inferred from these images that GO incorporation promotes the MG-63 cells adhesion and proliferation.

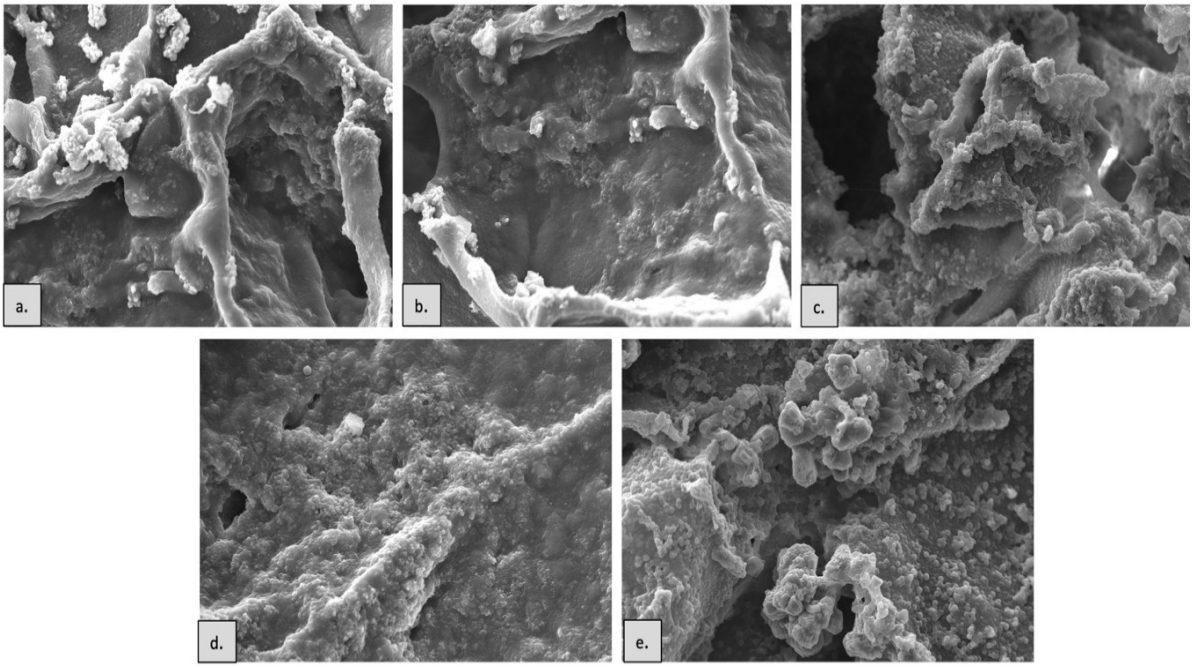

Figure 4.4.10: Cell spreading evaluation over developed scaffolds with GO nanoparticles and without GO nanoparticles (SEM Micrographs)

Table 4.1: Comparison among the developed scaffolds in the Dissertation

S.No.	Lyophilized Scaffold	Pore size (μm)	Porosity (%)	Mechanical Strength (MPa)	Degradation (%)	Swelling Index (mg/mL)	*In-vitro* Cell study
1.	Ch/G/0.02%CN	95	93	2.75	35	4	MG-63 cells, MTT, Live-dead assay
2.	Ch/G/nHAP/0.02% CN	121	83	2.89	81	5.93	MG-63 cells, MTT, Live-dead assay, ALP

3.	Ch/G/6%NBG/6%TCP	215.1	80	2.7	59	3	MG-63 cells, MTT, Live-dead assay, ALP
4.	Ch/G/NBG/60%GO	100	75.12	7.6	87	4.2	MG-63 cells ,MTT, Live-dead assay, ALP